VILNIUS UNIVERSITY

FACULTY OF PHYSICS

INSTITUTE OF PHOTONICS AND NANOTECHNOLOGY

Seda Türkcan

Carrier Dynamics in n-Gan/InGaN/p-GaN Structures with Different Active Layer Widths

MASTER'S THESIS

Photonics and Nanotechnology Study Program

Student	Seda Türkcan
Thesis supervisor	dr. Kazimieras Nomeika
Representative of the institute	prof. dr. Ramūnas Aleksiejūnas

Vilnius 2026

Contents

1 Introduction

Over the past few decades, III-Nitrides have emerged as a favorable material choice for optoelectronic devices, including light emitting diodes (LEDs), laser diodes and solar cells owing to their advantageous material properties including wide bandgap tunability, high mobility and thermal stability. External quantum efficiencies (EQE) of GaN-based blue LEDs reach values as high as 84%, while also offering broad spectral versatility by incorporation of aluminium (Al) and indium (In) [1].

Despite these advances, III-nitride semiconductor devices continue to face several critical limitations. One of the most significant challenges is the efficiency droop phenomenon observed at high carrier injection densities, which substantially degrades device performance. Furthermore, increasing the In composition in InGaN alloys leads to a pronounced reduction of quantum efficiency, thereby hindering the development of efficient green-emitting devices, commonly referred to as the "green gap" problem. In addition, III-nitrides exhibit strong intrinsic polarization effects arising from their crystal structure. This leads to significant spontaneous and piezoelectric polarization fields within heterostructures, particularly in quantum well (QW) systems. These internal electric fields induce the quantum-confined Stark effect (QCSE), which spatially separates electron and hole wavefunctions, reduces radiative recombination rates, and causes a redshift in the emission energy [2]. Consequently, the overall structural design of these structures plays a crucial role in determining the optical and electronic properties of the device.

The aim of this work is to investigate carrier dynamics in SQW InGaN structures with varying QW widths and cap layer doping configurations. Such a systematic study allows the individual effects of QW width and cap doping on carrier recombination and transport to be isolated, particularly their influence on internal polarization fields and QCSE. To achieve this, two complementary experimental techniques are employed: Light-Induced Transient Grating (LITG) and Time-Integrated Photoluminescence (TIPL). While previous studies have explored the influence of QW width on photoluminescence characteristics, a comprehensive analysis that simultaneously considers the interplay between well width and cap layer doping remains limited [3]. The present work addresses this gap through a systematic analysis of carrier lifetime, diffusion, and recombination mechanisms as a function of these structural parameters. The results offer further insights into the fundamental processes governing carrier dynamics in InGaN-based heterostructures and highlight potential pathways for mitigating efficiency losses and improving the performance of next-generation optoelectronic devices.

2 Theory

2.1 Carrier Recombination Mechanisms and the ABC Model

The optical and electronic properties of semiconductor materials are fundamentally governed by the dynamics of photo-generated charge carriers. Following optical excitation, non-equilibrium electrons and holes relax toward equilibrium through various recombination processes. Characterization of these mechanisms is essential for understanding carrier transport, evaluating internal quantum efficiency (IQE), and optimizing the performance of optoelectronic devices. Carrier recombination processes are generally classified as either radiative or non-radiative and are commonly described within the framework of the ABC recombination model. In its standard form, the ABC model considers three primary recombination pathways, as illustrated in Figure 1.

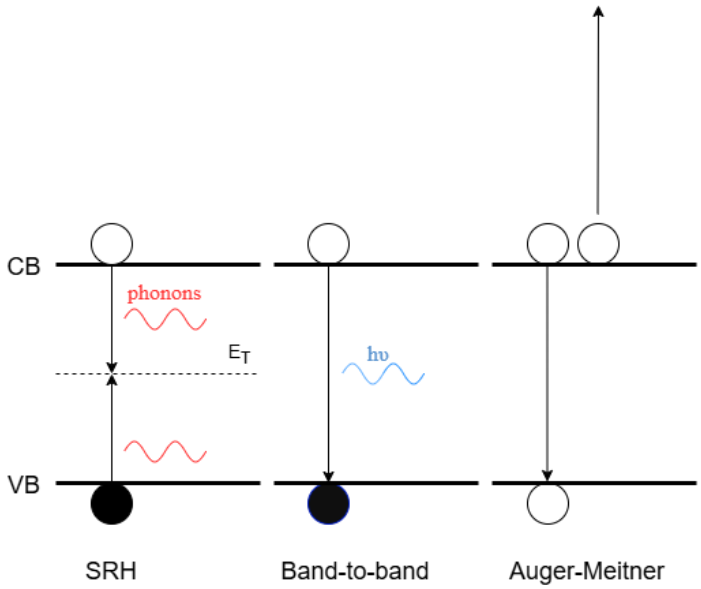

Figure 1. Charge carrier recombination mechanisms.

Shockley–Read–Hall (SRH) recombination is a non-radiative process mediated by defect or trap states located within the bandgap. In this mechanism, an electron or hole is first captured by a localized defect state, followed by recombination with a carrier of opposite charge. Since the recombination process is initiated through the capture of a single free carrier, the SRH recombination rate scales linearly with carrier density and may be expressed as:

$$R_A(n,p) = \frac{np}{\tau_p n + \tau_n p}, \tag{1}$$

where, τ_n and τ_p denote SRH lifetimes of electrons and holes, respectively, while n and p denote the non-equilibrium electron and hole densities.

Bimolecular recombination involves a direct recombination of an electron from conduction band (CB) and a hole from valance band (VB). When this recombination proceeds radiatively, it is referred to as band-to-band recombination, resulting in photon emission.

The rate of bimolecular recombination is expressed as:

$$R_B(n,p) = Bnp, \tag{2}$$

where B is bimolecular recombination coefficient. The efficiency of radiative recombination is strongly dependent on the overlap between electron and hole wavefunctions, which can be reduced in systems exhibiting carrier localization or internal field effects.

At high carrier densities, Auger–Meitner recombination becomes increasingly significant. In this non-radiative three-particle process, the recombination energy of an electron–hole pair is transferred to a third carrier rather than being emitted as a photon. The Auger–Meitner recombination rate is given by:

$$R_{C(n,p)} = C_n n^2 p + C_p n p^2 . \tag{3}$$

Here C_n and C_p are Auger-Meitner recombination coefficients for electron-electron-hole and electron-hole-hole processes, respectively. Due to its cubic dependence on carrier density, this mechanism becomes dominant under high injection conditions and is commonly associated with efficiency droop in semiconductor light-emitting devices.

Under high-injection conditions, the injected carrier density significantly exceeds the background doping concentration, allowing the approximation $n \approx p$. The overall carrier lifetime of the material is governed by all recombination mechanisms mentioned prior and can then be expressed by the equation:

$$\tau(n) = \frac{n}{R_A(n) + R_B(n) + R_C(n)} \tag{4}$$

The IQE is defined as the ratio of the radiative recombination rate to the total recombination rate. It can be expressed as:

$$IQE(n) = \frac{R_B(n)}{R_A(n) + R_B(n) + R_C(n)} . \tag{5}$$

The conventional ABC model provides a useful first-order description of recombination dynamics in many semiconductor systems. However, its validity relies on simplified assumptions such as

uniform carrier distributions, balanced electron–hole densities, and constant recombination coefficients. In practice, these assumptions may not fully hold in disordered or strongly excited semiconductor structures, where additional physical effects modify recombination kinetics.

2.1.1 Extended ABC Model

In realistic semiconductor heterostructures, especially those that have a lot of disorder like III-Nitrides, deviations from idealized conditions may arise due to residual doping, compositional fluctuations, defect states, and spatial carrier inhomogeneities. As a result, the assumption $n = p$, commonly employed in the conventional ABC model, may no longer remain strictly valid. To account for such effects, a background electron density n_0 is introduced, representing residual or equilibrium carrier populations present within the structure. The SRH, bimolecular, and Auger–Meitner recombination contributions can then be reformulated as:

$$R_A(n) = \frac{(n + n_0)n}{\tau_p(n + n_0) + \tau_n n}, \tag{6}$$

$$R_B(n) = Bn(n + n_0), \tag{7}$$

$$R_C(n) = C_n n(n + n_0)^2 + C_p n^2(n + n_0). \tag{8}$$

In addition to background carrier effects, non-radiative recombination pathways may be enhanced in disordered semiconductor systems. In particular, trap-assisted Auger–Meitner (TAAM) recombination has been identified as an additional loss mechanism, where two free carriers recombine while transferring their excess energy to a carrier trapped in a defect state, as illustrated in Figure 2. Unlike conventional Auger–Meitner recombination, the TAAM process exhibits a quadratic dependence on carrier density, analogous to the bimolecular contribution described by equation (7). Consequently, TAAM-related losses may be incorporated to equations (4) and (5) through an effective bimolecular recombination coefficient defined as: B* = B_{rad} + B_{TAAM} that accounts for the TAAM recombination and diffusion-driven losses [4], [5] .

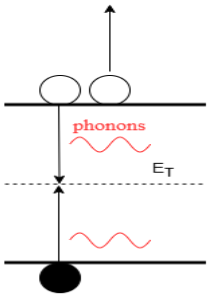

Figure 2. Trap-assisted Auger Meitner recombination mechanism.

At high carrier densities, further deviations from ideal recombination behavior arise due to phase-space filling effects and the transition from Maxwell–Boltzmann to Fermi–Dirac carrier statistics. In this regime, the finite availability of electronic states leads to saturation of the radiative recombination coefficient, which can be expressed as:

$$B_{rad}(n) = \frac{(\mathrm{B}_{0rad})}{1 + \frac{n}{n_{sat}}} \ , \tag{9}$$

here, B_{0rad} is the low-injection radiative recombination coefficient in the absence of saturation and n_{sat} denotes a characteristic non-equilibrium carrier density at which B_{0rad} decreases to half of its initial value. Such effects have been widely reported to influence recombination efficiency under high excitation conditions [6].

Similarly, the occupation of defect states evolves with carrier injection. At low carrier densities, empty trap states efficiently capture carriers, resulting in reduced carrier lifetimes. As the carrier density increases, these states become progressively filled, reducing their effective capture probability and leading to an apparent increase in lifetime. This behavior can be incorporated phenomenologically by introducing a density-dependent SRH lifetime. This saturation behavior is integrated into the model by adjusting the carrier lifetimes τ_n and τ_p in equation (6) accordingly:

$$\tau_{n_0,p_0} = \tau_{n_0,p_0}\left(1 + \frac{n_{SRH}}{\mathrm{n}}\right) \tag{10}$$

where, n_{SRH} is the characteristic density at which the lifetime reaches approximately half of its low-injection value.

The recombination mechanisms described above directly influence experimentally measurable quantities such as carrier lifetime, carrier diffusion length, and photoluminescence intensity. Since each recombination pathway exhibits a distinct dependence on carrier density, analysis of carrier lifetime and IQE enables experimental identification of the dominant recombination mechanisms and extraction of effective ABC recombination coefficients.

3 Literature Review

3.1 Properties of III-Nitrides

Indium Gallium Nitride (InGaN) is a ternary III–V semiconductor in III-Nitride family, formed by alloying Indium Nitride (InN) and Gallium Nitride (GaN). GaN is a wide bandgap semiconductor with a direct bandgap energy of approximately 3.4 eV, while InN has a significantly narrower bandgap of about 0.7 eV. By varying the In composition x in $In_xGa_{1-x}N$, the bandgap can be tuned across a broad spectral range spanning the visible region, making it highly suitable for optoelectronic applications such as light-emitting diodes (LEDs), laser diodes, and photovoltaic devices.

Both GaN and InN can crystallize in either the zinc blende or hexagonal wurtzite crystal structures; however, the wurtzite phase, illustrated in Figure 3, is thermodynamically more stable and is therefore predominantly employed in device fabrication [7]. In hexagonal structure, the lattice is described by two parameters, *a* (in-plane) and *c* (out-of-plane). Since epitaxial growth typically occurs along the c-axis, lattice mismatch is defined using the in-plane lattice parameter *a*, as it governs the strain at the growth interface, while the *c* parameter adjusts in response to this strain.

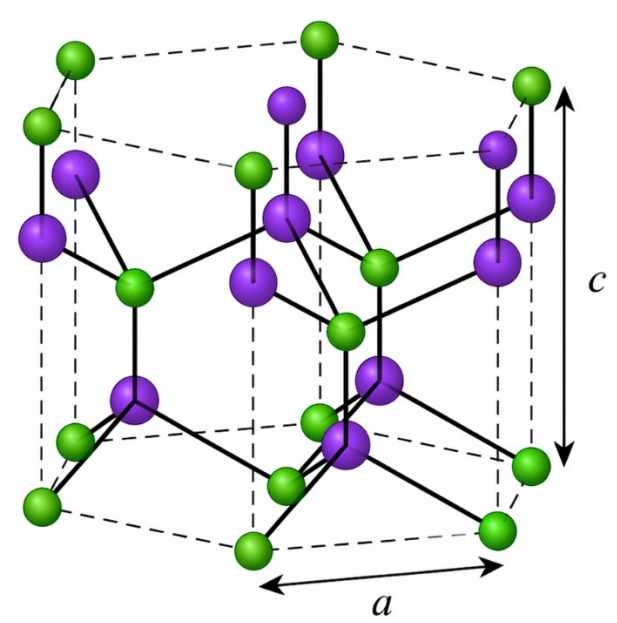

Figure 3. Wurtzite structure of III-Nitrides.

A key challenge in InGaN material growth arises from the substantial lattice mismatch between GaN (a ≈ 3.189 Å) and InN (a ≈ 3.545 Å), which is approximately 11% [8]. This mismatch induces biaxial strain in the epitaxial layers, which can be either compressive or tensile depending on the relative lattice parameters of the materials involved. In the case of InGaN grown on GaN, the larger

lattice constant of InGaN results in compressive in-plane strain, while the lattice expands along the c-axis in response. Such strain strongly influences the electronic band structure and internal polarization fields, while also promoting defect formation, phase separation, and compositional inhomogeneity during epitaxial growth [9].

Additionally, lattice mismatch between GaN and commonly used substrates further complicates epitaxial growth. Bulk GaN substrates provide the closest lattice compatibility and therefore enable growth of high-quality epitaxial layers with relatively low threading dislocation densities. However, their high cost and limited availability restrict widespread industrial adoption. Silicon carbide (SiC) substrates also offer a small lattice mismatch with GaN (approximately 3%) together with high thermal conductivity (3.7 W/cm K) and electrical conductivity, enabling efficient heat dissipation. However, it is challenging to handle and polish SiC, hindering its effective production [10]. As a result, sapphire remains the most widely used substrate for III-nitride device fabrication due to its optical transparency, chemical stability, and comparatively low cost. However, sapphire exhibits a substantial lattice mismatch with GaN of approximately 16%, leading to significant strain accumulation and the formation of structural defects such as threading dislocations (TDs) and stacking faults during growth [11]. Threading dislocations generally act as non-radiative recombination centers (NRC) and are therefore expected to reduce device efficiency. Despite afore mentioned issues, InGaN-based blue LEDs still achieve high IQE. One explanation is that the V-shaped pits forming at TD sites act as barriers that prevent carriers from reaching non-radiative recombination centers, effectively reducing their impact [12]. Nonetheless, the exact role of TDs in device performance remains under debate.

3.2 Growth of InGaN/GaN Structures

InGaN is typically employed in the form of thin-film layers or quantum wells (QWs), which are commonly grown using epitaxial techniques such as molecular beam epitaxy (MBE) or metal-organic chemical vapor deposition (MOCVD). Among these, MOCVD is the preferred technique for the epitaxial growth of InGaN due to its advantages in achieving rapid growth rates, and suitability for large-scale production. In MOCVD, metal-organic precursors such as trimethylgallium (TMGa) and trimethylindium (TMIn) are introduced in vapor form to a heated substrate using carrier gases like H_2 or N_2. Ammonia (NH_3) serves as the nitrogen source. Magnesium and silicon doping is achieved using bis(cyclopentadienyl)magnesium (Cp_2Mg) and silane (SiH_4), serving as p-type and n-type dopant sources, respectively [7]. Growth temperature

needed for GaN is 1000 °C while for InGaN, temperatures have to be kept below 800°C [13]. This large temperature disparity, combined with the ~11% lattice mismatch between InN and GaN [8], makes it challenging to incorporate In uniformly during InGaN growth. As a consequence, several composition-related phenomena arise during growth. In tends to segregate, leading to the formation of regions with locally elevated In content. These compositional fluctuations create potential minima that can localize charge carriers. While such carrier localization may enhance radiative recombination efficiency by reducing the influence of nonradiative defects, it can also impede carrier transport and contribute to spectral inhomogeneity, particularly at higher In contents [14].

In addition, strain-induced effects give rise to the so-called composition pulling effect, wherein the incorporation of In is reduced in the initial stages of growth due to compressive strain, and gradually increases as strain relaxation occurs. This results in a non-uniform In distribution along the growth direction of the layer or QW. Theoretical and experimental studies, such as those by Inatomi et al. [15] and Gerald B. Stringfellow [16], have shown that this effect plays a significant role in determining the compositional profile and microstructure of InGaN layers.

Therefore, precise control over growth conditions and strain management is essential to achieve uniform In incorporation and optimize the optical and electronic properties of InGaN-based devices.

3.2.1 Doping and Defect Formation During Growth

The optical and electronic properties of InGaN/GaN heterostructures are also significantly influenced by both native point defects and intentional doping. Native defects, which are intrinsic to the crystal structure, form during epitaxial growth and play a key role in determining conductivity and compensation behavior. The most prominent native defects are nitrogen vacancies (V_{N}) and gallium vacancies (V_{Ga}). V_N generally acts as shallow donor state and is commonly associated with unintentional n-type conductivity [17], particularly under gallium-rich growth conditions. In contrast, V_{Ga} typically behaves as a deep acceptor and is more likely to form in p-type layers grown under nitrogen-rich environments [18]. The inherent background n-type conductivity observed in GaN and InGaN is primarily attributed to the presence of V_N.

Intentional n-type doping in GaN and InGaN is commonly achieved using silicon (Si), owing to its relatively low activation energy and efficient incorporation into the crystal lattice. In MOCVD

growth, Si is typically introduced using silane (SiH_4) or disilane (Si_2H_6) precursor gases. In contrast, achieving reliable p-type conductivity remains considerably more challenging. Magnesium (Mg) is the most widely used acceptor dopant; however, its relatively high activation energy (180 meV) limits the achievable hole concentration at room temperature. Furthermore, hydrogen originating from carrier gases and precursor decomposition may form electrically inactive Mg–H complexes, leading to passivation of Mg acceptors during growth [19], [20]. Despite recent advancements such as post-growth rapid thermal annealing (RTA) to dissociate Mg–H complexes and activate p-type conductivity, high Mg doping levels on the order of 10^{20} cm^{-3}, to obtain a hole concentration of ~10^{18} cm^{-3} at room temperature is still needed. Such high Mg incorporation may also introduce additional structural defects, strain, and defect complexes within the material. Moreover, Mg diffusion and segregation during epitaxial growth can lead to partial incorporation of Mg into adjacent layers, including the quantum well region. Such effects may introduce additional non-radiative recombination centers, alter local electric fields, and influence carrier localization and transport within InGaN QWs.

3.3 Polarization Fields in InGaN and QCSE

A fundamental challenge in InGaN heterostructures arises from the intrinsic polarity of the wurtzite lattice, which lacks inversion symmetry. This asymmetry defines a unique crystallographic direction along the c-axis ([0001]), referred to as the polar axis. Because of the polar lattice structure and the difference in electronegativity between group-III and nitrogen atoms, a finite spontaneous polarization P_{sp} exists along this direction. First-principles calculations by Bernardini et al. demonstrated [2] polarization in III-nitrides is significantly larger than in conventional III–V semiconductors.

In addition, lattice mismatch between InGaN and GaN layers introduces strain within the epitaxial heterostructure. Due to the non-centrosymmetric nature of the wurtzite crystal structure, this strain distorts the crystal lattice and induces an additional polarization component known as piezoelectric polarization, P_{pz}. In strained InGaN/GaN QWs, piezoelectric polarization may become comparable to or even exceed the spontaneous polarization contribution depending on In composition and strain state. The total polarization may therefore be expressed as:

$$P_{tot} = P_{sp} + P_{pz}. \tag{11}$$

Spatial discontinuities of polarization at heterointerfaces give rise to fixed sheet charges, which generate strong internal electric fields within the QW regions. Theoretical studies predict that these built-in electric fields may reach magnitudes on the order of MV/cm in strained III-nitride quantum wells. These fields significantly modify the band structure, resulting in band bending and the spatial separation of electron and hole wavefunctions. This phenomenon is known as the quantum-confined Stark effect (QCSE).

Under the influence of QCSE, electrons and holes are driven toward opposite interfaces of the QW, reducing their spatial overlap and consequently decreasing the probability of radiative recombination. In addition, the effective transition energy is reduced due to the tilted potential profile, leading to a redshift in the emission wavelength. These effects become increasingly pronounced in wider QWs and at higher In compositions due to enhanced strain and stronger polarization fields. Experimental studies by Chichibu et al. [14] demonstrated that polarization-induced carrier separation strongly influences the optical properties and recombination dynamics of InGaN QWs. Figure 4 illustrates the influence of internal electric fields on the electronic structure of InGaN/GaN QWs. In the absence of polarization fields, electron and hole wavefunctions exhibit substantial spatial overlap. However, in wider QWs containing strong internal electric fields, significant band tilting and carrier separation occur, resulting in reduced overlap between electron and hole wavefunctions. In narrower quantum wells, the influence of the internal electric field is partially suppressed due to stronger quantum confinement and reduced carrier separation distance.

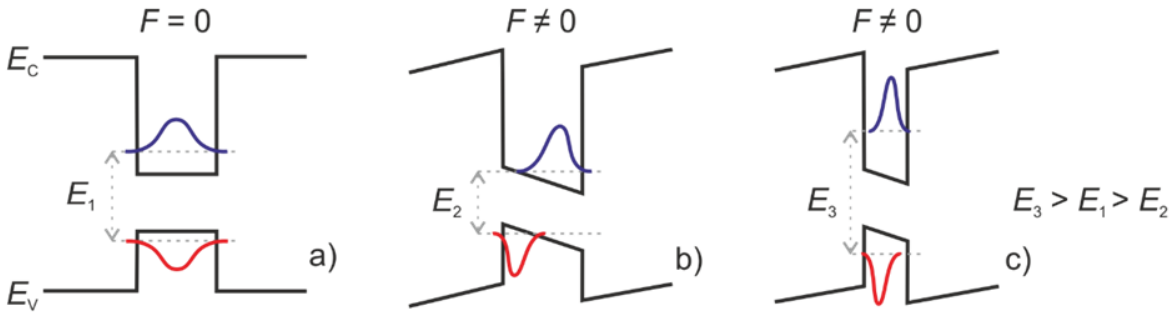

Figure 4. First energy levels of electrons and holes and their wave functions: in a wide QW without internal fields (a), in a wide QW with internal fields (b), and in a narrow QW with internal fields (c). Taken from [4].

At high carrier injection densities, the internal electric fields can be partially screened by the accumulated charge carriers. This screening reduces band bending and weakens the QCSE,

typically resulting in a blueshift of the emission energy with increasing excitation or current density [21].

3.3.1 Mitigation of Polarization Fields

Several approaches have been proposed to mitigate the effects of internal polarization fields in III-nitride heterostructures. One of the most direct strategies involves the growth of nonpolar or semipolar orientations of GaN and InGaN. In nonpolar structures, such as the m-plane $(10\bar{1}0)$ and a-plane $(11\bar{2}0)$, the polarization vector lies parallel to the growth plane, effectively eliminating the internal electric field along the quantum well direction [22]. In semipolar orientations, including planes such $(11\bar{2}\bar{4})$ and $(10\bar{1}2)$, the polarization vector is inclined relative to the growth direction, resulting in a reduced or even nullified fields [23]. These configurations significantly suppress the quantum-confined Stark effect (QCSE), improving electron–hole wavefunction overlap and enhancing radiative recombination efficiency.

In addition to orientation, the inherent polarity of the material provides a second lever for field manipulation. In wurtzite GaN, growth along the c-axis can occur in either the Ga-polar ([0001]) or N-polar ($[000\bar{1}]$) direction, corresponding to surfaces terminated by gallium or nitrogen atoms, respectively. While Ga-polar growth is conventional due to its superior surface morphology, N-polar growth has gained interest for its ability to reverse the direction of polarization fields. This reversal modifies band bending and carrier confinement in ways that can benefit specific device architectures. However, N-polar epitaxy is significantly more challenging due to lower surface mobility of Ga adatoms on the N-polar face, resulting in hexagonal hillocks, which degrades surface planarity [24].

More recently, engineering surrounding barriers and cap layers has been proposed as a method to influence internal electric fields [25]. In particular, p-type GaN (p-GaN) cap layers can introduce additional built-in electric fields associated with ionized Mg acceptor dopants, which can modify the local potential profile near the QW region [26], [27]. Depending on the doping profile, these fields can be engineered to partially compensate for intrinsic polarization, effectively flattening the energy bands. In contrast, unintentionally doped GaN (u-GaN) cap layers exhibit significantly lower fixed charge density and therefore induce weaker perturbations of the QW potential. Consequently, cap layer design can influence carrier confinement, wavefunction overlap, carrier transport, and recombination dynamics in InGaN/GaN quantum well structures.

4 Experimental Methods

4.1 Sample Information

In this study, eight InGaN single quantum well (SQW) samples were designed and investigated, with the QW thickness and cap layer doping intentionally varied as the primary experimental parameters. The structures were grown using the MOCVD technique by A. Kadys at Vilnius University, Institute of Photonics and Nanotechnology.

The SQW thicknesses were 2, 3, 5, and 7 nm, selected to systematically probe quantum confinement effects and strain-related modifications in the active region. In parallel, two types of cap layers—unintentionally doped GaN (u-GaN) and p-type GaN—were implemented to investigate how cap layer doping modifies the internal electric field distribution, with the hypothesis that p-type doping may partially screen or even reverse the built-in polarization field, thereby altering carrier recombination dynamics in a manner analogous to a p–n junction. A schematic representation of the sample structure is shown in Figure 5.

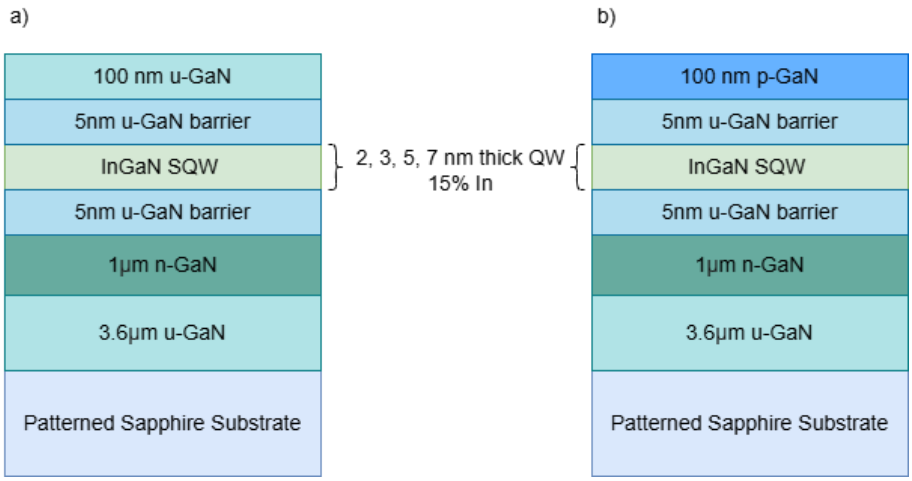

Figure 5. Structure of a) InGaN SQWs with u-GaN cap layer and b) InGaN SQWs with p-GaN cap layer.

Each sample was grown on a patterned sapphire substrate (PSS) to reduce threading dislocation density (TDD) and enhance light extraction efficiency. The epitaxial structure consists of a 3.6 µm undoped GaN (u-GaN) template, followed by a 1 µm Si-doped n-GaN layer. The active region comprises a single InGaN SQW with a nominal In composition of 15%, embedded between two 5 nm low-temperature GaN (LT-GaN) barrier layers. To preserve the structural integrity of the active region, the InGaN SQW was grown at 800 °C (810 °C for the 7 nm sample). The LT-GaN barriers were deposited at the same growth temperature as the SQWs.

Due to the relatively low growth temperature, the LT-GaN barriers are expected to exhibit an elevated defect concentration compared to conventionally grown GaN layers, with reported values in the literature typically ranging from approximately 10^{17} to 10^{19} cm^{-3} [28]. Similarly, the InGaN SQW region may also possess a relatively high nominal n-type background concentration within a comparable range. Such elevated defect and background carrier concentrations could also reduce carrier mobility within the active region.

The SQW thickness was precisely controlled via growth duration, with deposition times of 81, 121, 202, and 283 s corresponding to nominal thicknesses of 2, 3, 5, and 7 nm, respectively. Finally, a 100 nm cap layer (u-GaN or p-GaN) was deposited at 830 °C (840 °C for the 7 nm sample) to complete the structures. To activate the Mg of p-GaN cap layers, at the end of growth process, samples were annealed for 30 s at 850°C. Annealing procedure was also applied to u-GaN cap samples to have same impacts on the QWs. The sample set and corresponding naming scheme are summarized in Table 1 and are used throughout this thesis.

Table 1. Sample information and their representation in this thesis

Sample Name	Cap Layer	QW Thickness (nm)	Growth Temperature (C)	Growth Duration (s)
U-2	u-GaN	2	800	81
P-2	p-GaN			
U-3	u-GaN	3	800	121
P-3	p-GaN			
U-5	u-GaN	5	800	202
P-5	p-GaN			
U-7	u-GaN	7	810	283
P-7	p-GaN			

4.2 Time Integrated Photoluminescence and QE Measurement

TIPL is a spectroscopic technique used to measure the total light emitted from a sample over a defined time interval following optical excitation. To ensure radiative recombination, the sample is excited with photons whose energy exceeds its bandgap, promoting electrons from the valence band to the conduction band. The resulting emission is then collected by a spectrometer for spectral analysis.

The experimental setup depicted in Figure 6 utilizes a femtosecond laser system (PHAROS, Light Conversion) operating at a wavelength of 1030 nm, with a pulse duration of 250 fs and a repetition rate of 30 kHz. The output is routed through an optical parametric amplifier (OPA, ORPHEUS, Light Conversion) and frequency-doubled via a second harmonic generation (SHG) crystal to produce 385 nm excitation wavelength. The laser beam then passes through a gradient filter to modulate excitation intensity before being focused onto the sample. For standard spectral characterization over a wide range of intensities, particularly at low excitation where signal-to-noise ratios are critical, the PL signal was collected using a focusing lens coupled to a fiber spectrometer (AvaSpec-ULS2048, Avantes). This configuration mitigates detector saturation while improving detection limits at long integration times.

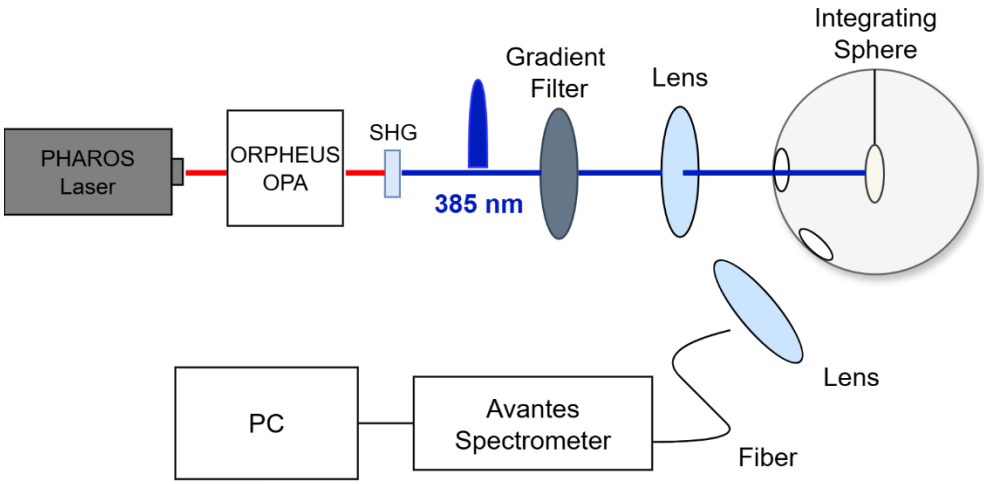

Figure 6. TIPL setup for measurement of multiple excitation fluences.

To evaluate emission efficiency and charge carrier recombination mechanisms, TIPL measurements were paired with an integrating sphere (Gigahertz-Optik) coated with $BaSO_4$ for high diffuse reflectivity as shown in Figure 7. This allows for the calculation of the Internal Quantum Efficiency (IQE), defined as the ratio of emitted photons to absorbed photons. For this, fiber spectrometer was directly connected to the integrating sphere to measure the photon count within the sphere.

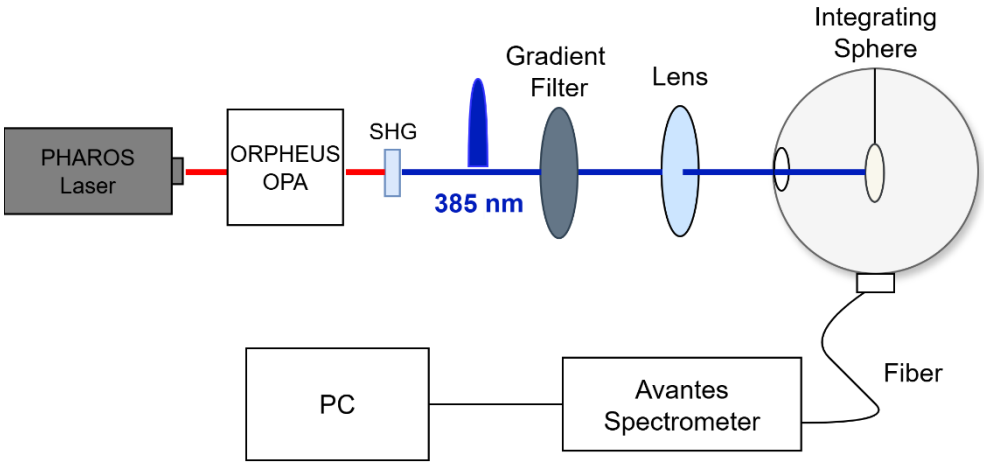

Figure 7. QE measurement setup.

For IQE measurement, two configurations are typically employed: one with the sample placed inside the integrating sphere and one with an empty sphere. IQE is then calculated as the following expression:

$$IQE = \frac{P_c}{L_a - L_c}, \tag{12}$$

where P_c is the number of photons in photoluminescence spectral region, measured when sample is inside the integrating sphere, L_c is the number of photons in the spectral region of the laser line when sample is inside the sphere and L_a is the number of photons in laser line with empty sphere. The number of photons in each spectral region is determined by integrating the corrected spectra. This is done by multiplying the measured spectra by wavelength and the appropriate calibration curve and normalizing by the corresponding integration time to account for measurement conditions.

To ensure high accuracy and account for indirect absorption effects (such as scattering or secondary reflections from the sphere walls), this study adopts the three-measurement configuration suggested by Leyre et al. [29]:

1. Configuration A: Reference measurement of the empty integrating sphere.
2. Configuration B: Sample placed inside the sphere but kept out of the direct excitation beam path.
3. Configuration C: Sample placed inside the sphere and directly in the excitation beam path.

The inclusion of the second measurement accounts for indirect absorption effects such as scattering or reflection of the excitation light by the sample or the sphere wall, which could otherwise lead

to inaccuracies in the calculated IQE. The experimental configurations are illustrated in Figure 8, and an example spectrum is presented in Figure 9. IQE in three-measurement approach is calculated by the following formula:

$$IQE = \frac{P_C - (1 - A_{dir})P_b}{L_a A_{dir}}, \tag{13}$$

Where P_b is the number of photons in photoluminescence region for sample out of the path of excitation beam (intensity of photoluminescence from indirect absorption) and A_{dir} in the formula represents the amount of directly absorbed light, which is given by:

$$A_{dir} = 1 - \frac{L_c}{L_b}. \tag{14}$$

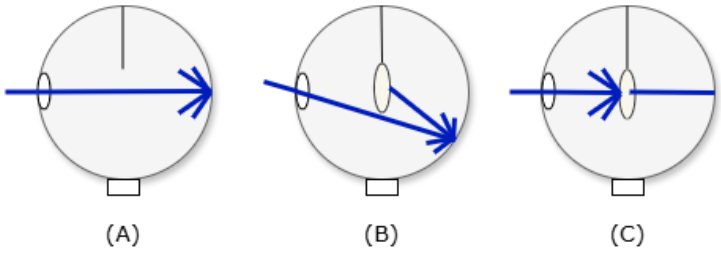

Figure 8. Three-measurement approach for calculation of IQE: (A) empty sample configuration, (B) measurement with sample out of the path of the beam, (C) measurement with sample in the path of the beam.

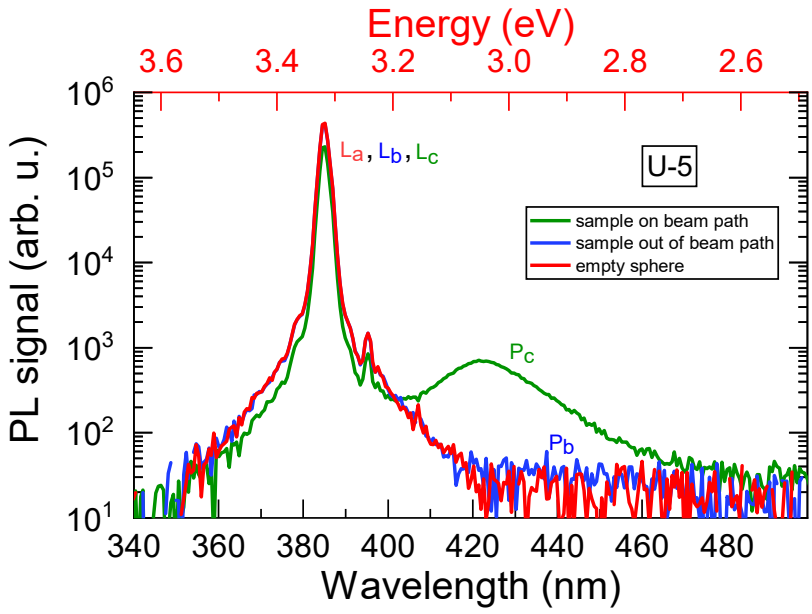

Figure 9. Spectra of U-5 sample in A, B and C configurations.

It is important to note that, while the three-measurement approach provides reliable results for liquid samples and single-layer spin-coated systems, its direct application to solid-state thin-film structures introduces additional complexities. In particular, light extraction and reabsorption losses associated with the Stokes shift must be considered, especially for GaN-based samples where the Stokes shift is small. These effects are not accounted for in standard IQE measurements and can therefore lead to a significant underestimation of the true IQE.

As a result, the values obtained for thin solid-state samples should be regarded as a quasi-quantum efficiency (quasi-QE) rather than the intrinsic IQE. To correct for reabsorption losses, TIPL measurements performed outside the integrating sphere can be compared with measurements inside the sphere by aligning the long-wavelength side of the spectra. In addition, losses related to photon extraction can be addressed using optical ray-tracing simulations. Combining these approaches enables a more realistic assessment of photon recycling and escape probabilities, leading to a more accurate estimation of the true internal quantum efficiency.

4.3 LITG Technique

LITG is a special pump–probe technique in which two coherent pump beams intersect at an angle θ, forming an interference pattern that generates a spatially periodic excitation of non-equilibrium charge carriers, or transient grating, within the sample. These carriers induce a temporary modulation of the material's refractive index as per Drude theory [30]. According to this model, the change in the refractive index is related to the density of the generated free carriers:

$$\Delta n = -\left(\frac{e^2 {\lambda_p}^2}{8\pi^2 c^2 \varepsilon_0 n_0}\right)\left(\frac{N}{m_e} + \frac{P}{m_h}\right) = \Delta N^* n_{eh}\,, \tag{15}$$

where λ_p is the pump wavelength, n_0 is the initial refractive index, N and P are the electron and hole densities, and m_e and m_h are their effective masses. ΔN denotes the total photoexcited carrier density, and n_{eh} represents the refractive index change per electron–hole pair. This modulated sample excitation acts as a transient diffraction grating, which is detected by a probe beam. The fundamental scheme of LITG technique is represented in Figure 10. The period of the transient grating depends on the angle between the two pump beams and is given by:

$$\Lambda = \frac{\lambda_p}{2\sin\left(\frac{\theta}{2}\right)} \tag{16}$$

The probe beam is only partially diffracted, and the diffraction efficiency can be exhibited as intensity ratio η between the diffracted I_D and the transmitted I_T parts of it, which is mathematically represented in the following manner:

$$\eta(\Delta t) = \frac{I_D}{I_T} = \left(\frac{\pi d n N}{\lambda}\right)^2 \exp\left(-\frac{2\Delta t}{\tau_G}\right)^2 \tag{17}$$

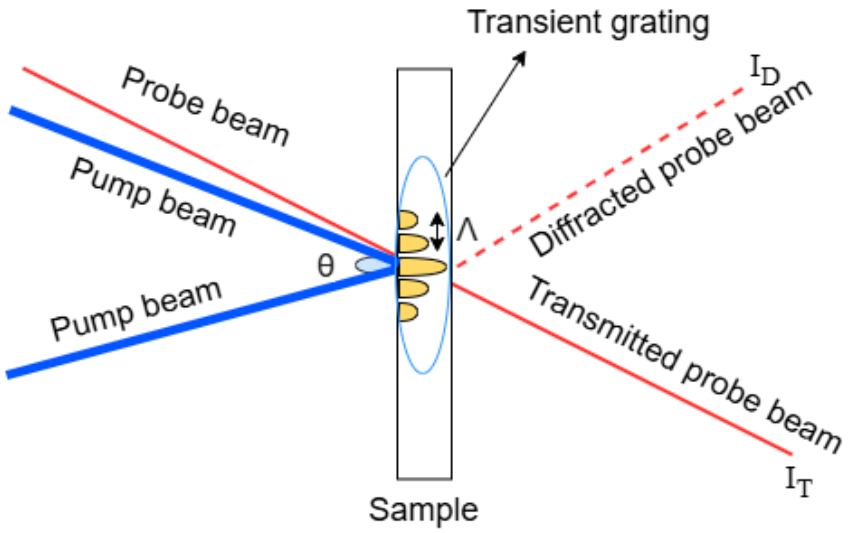

Figure 10. Principle of LITG technique.

LITG measurements are typically performed in transmission mode by detecting the diffracted probe beam passing through the sample. However, in this study, the investigated SQW samples were grown on patterned substrates and were initially unpolished. Although the samples were subsequently polished to enable LITG measurements, diffraction effects originating from the substrate patterning significantly reduced the transmitted probe signal, rendering it comparable to the background noise level. As a result, reliable detection in transmission geometry was not feasible. Therefore, all measurements were carried out in reflection mode, where the diffracted probe beam is detected from the same side as the incident excitation and probe beams.

The experimental setup is illustrated in Figure 11. A femtosecond laser system (CARBIDE, Light Conversion) operating at a central wavelength of 1030 nm, with a pulse duration of 200 fs and a repetition rate of 100 kHz, was used as the excitation source. The laser output was directed into an optical parametric amplifier (OPA, ORPHEUS, Light Conversion), generating a pump beam at 385 nm, while the fundamental wavelength (1030 nm) was retained as the probe beam. The pump wavelength was selected to efficiently excite the InGaN active layer, as it lies well above its bandgap energy, while minimizing excitation of the underlying GaN layers and substrate. LITG measurements were performed using a HARPIA-TG transient grating spectrometer (Light

Conversion), which enables characterization of carrier dynamics through the temporal decay of the diffraction signal from the induced transient grating. Within the HARPIA-TG system, a wollaston prism is used to separate the pump beam into two coherent pump beams. A motorized mirror (M1) is used to control the optical alignment and adjust the transient grating period. The same mirror also collects the diffracted probe beam (indicated by a dashed line in Figure 10) and directs it to a detector, where the signal is recorded and subsequently transferred to a computer for analysis.

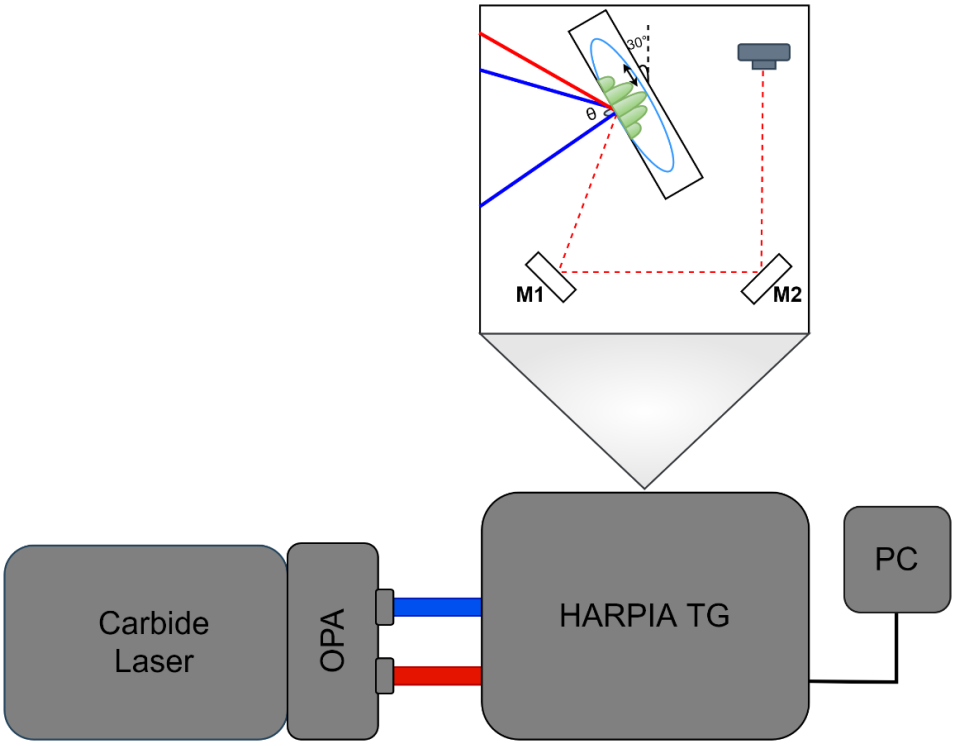

Figure 11. Experimental setup used for LITG measurements in reflection mode.

Due to the experimental constraints discussed previously, measurements were conducted in reflection mode. In this configuration, only the diffracted probe beam can be detected, as transmission through the sample is not accessible, hindering direct determination of the diffraction efficiency. Furthermore, the internal geometry of the HARPIA-TG system requires the sample to be tilted during reflection-mode measurements. A tilt angle of 30° was selected to maximize the accessible range of transient grating periods. As a consequence of this inclined geometry, the grating period calculated using the standard expression (Equation 16) must be corrected by a factor of $\cos^{-1}(30°)$ to account for projection effects.

The transient grating signal is monitored via the change in the diffracted probe intensity, from which the grating decay rate $\frac{1}{\tau_G}$ can be extracted. This decay is governed by two primary processes: carrier recombination and carrier diffusion, and can be expressed as:

$$\frac{1}{\tau_G} = \frac{1}{\tau_R} + \frac{1}{\tau_D} = \frac{1}{\tau_R} + D\left(\frac{2\pi}{\Lambda}\right)^2, \tag{18}$$

where $\tau_R$is the carrier recombination lifetime, D is the carrier diffusivity, and $\Lambda$is the transient grating period.

This relation indicates that the grating decay rate depends on the grating period: shorter grating periods correspond to larger spatial frequency $\frac{2\pi}{\Lambda}$, resulting in faster decay due to enhanced diffusion. The decay dynamics measured at different grating periods at the same excitation fluence are shown in Figure 12a. By performing measurements at different fluences over a range of grating periods, a linear dependence of $\frac{1}{\tau_G}$ on $\frac{2\pi}{\Lambda}$ is obtained, as illustrated in Figure 12b.

From this linear relationship, the carrier diffusivity D is determined from the slope, while the intercept at $(2\pi/\Lambda)^2 = 0$ yields the inverse carrier lifetime $1/\tau_R$. Once both D and τ_R are known, the carrier diffusion length L_D can be calculated as:

$$L_D = \sqrt{D\tau_R}\,. \tag{19}$$

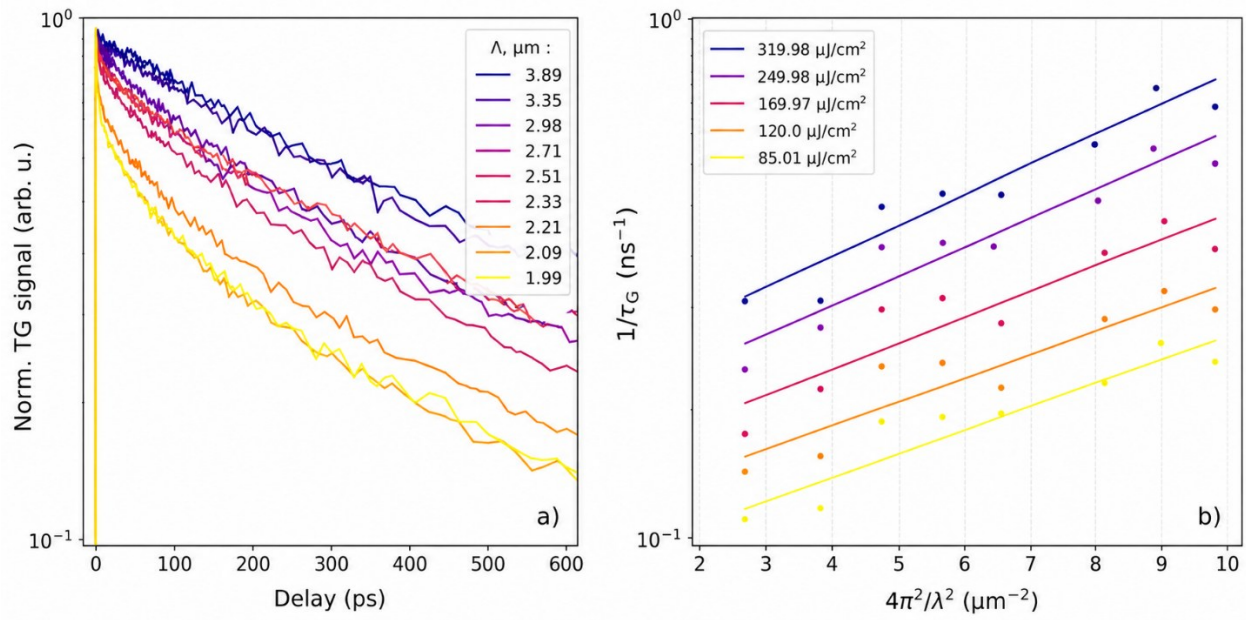

Figure 12. a) LITG decay kinetics kinetics at $320\,\frac{\mathrm{uJ}}{\mathrm{cm}^2}$ for sample U-7 b) Inverse decay time $\frac{1}{\tau_G}$ as a function of different grating periods for sample U-7.

5 Results and Discussion

5.1 TIPL Results

TIPL measurements were performed as a function of excitation fluence (0.5–2500 μJ/cm²), as shown in Figure 13. For the 2 nm SQWs, both u-GaN and p-GaN capped samples exhibit a single dominant emission peak across all fluences, indicating recombination from the ground-state transition, with peak emission at 430 nm.

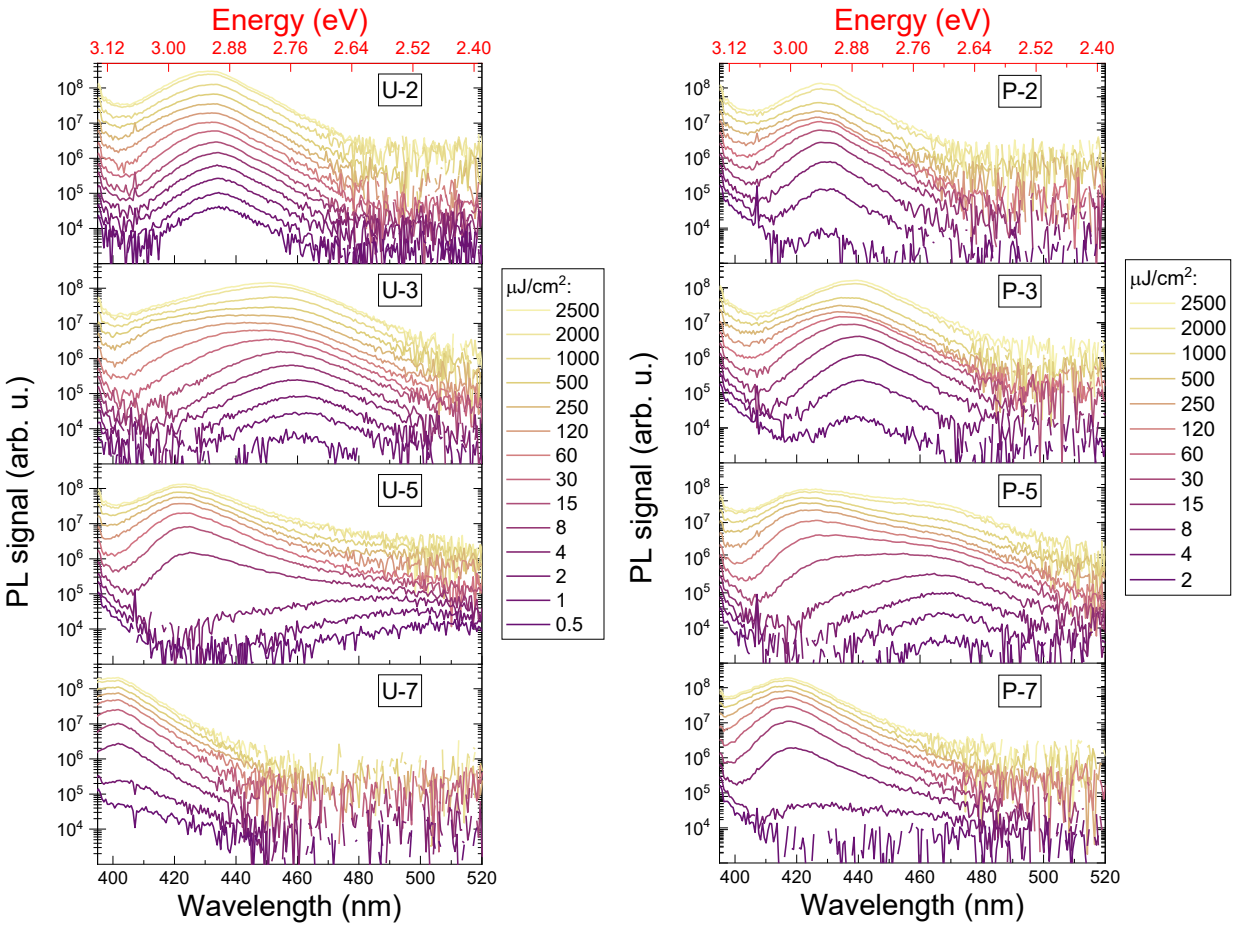

Figure 13. TIPL plots of samples with u-GaN cap (left) and p-GaN cap (right).

With increasing QW thickness (3–5 nm), a clear red shift is observed. While strong quantum confinement in 2 nm QW structures partially suppress QCSE induced redshift, the reduced overlap of electron and hole wavefunctions no longer allows this for 3 and 5 nm QWs. In addition, emergence of double-peak emission is also observed. The appearance of these double emission peaks suggests coexistence of two recombination channels: (i) delocalized or weakly localized states corresponding to the QW band structure, and (ii) strongly localized states associated with In-rich clusters or potential fluctuations [31] [32]. This behavior is closely related to the epitaxial

growth dynamics of the InGaN/GaN system. Due to the lattice mismatch between InGaN and GaN, the InGaN layer is initially compressively strained to match the GaN template, resulting in a compositional pulling effect that suppresses In incorporation during the early growth stages. Consequently, the actual In concentration is lower than expected from the precursor gas flow ratios alone. As the QW thickness increases, accumulated strain partially relaxes through the formation of defects such as misfit dislocations. This relaxation could promote In segregation and phase separation, producing In-rich clusters with narrower local bandgaps that act as carrier localization centers. Recombination within these localized regions gives rise to the lower-energy emission peak, while recombination from QW band structure contributes to the higher-energy peak. Similar observations were reported by Zhu et al. [33]. It is also observed that, relative contribution of these recombination channels depends strongly on excitation fluence. At low excitation densities, carriers preferentially occupy localized states, whereas increasing excitation leads to their saturation and promotes recombination from higher-energy delocalized states. In addition, carrier-induced screening of the internal piezoelectric field at elevated carrier densities further modifies the emission characteristics. For the 7 nm SQW samples, the emission peak exhibits a slight blue shift relative to the lower QW width counterparts for both u-GaN and p-GaN structures. This shift may be attributed to the higher growth temperature employed for the 7 nm QWs, which could enhance In desorption during growth and consequently reduce the effective In incorporation within the QW.

To further analyze the spectral dynamics, peak emission wavelength λ_{peak} and FWHM are plotted as a function of the generated carrier density. The photogenerated carrier density immediately after laser excitation is estimated using the formula:

$$N = \frac{(1-R)\alpha\lambda I_0}{hc} \tag{20}$$

where N is the generated carrier density, R is the surface reflectivity (taken as 0.21 for InGaN), λ is the excitation wavelength, and I_0 is the incident excitation fluence. The constants h and c denote Planck's constant and the speed of light, respectively. The absorption coefficient α depends on the In composition of the InGaN layer; for a nominal In content of 15%, the value of 1.5×10^5 cm^{-1} is adopted based on literature reports for similar structures [34].

Resulting plots of λ_{peak} as a function of carrier density for u-GaN and p-GaN cap samples are represented in Figure 14. The influence of the cap layer remains evident across all QW thicknesses.

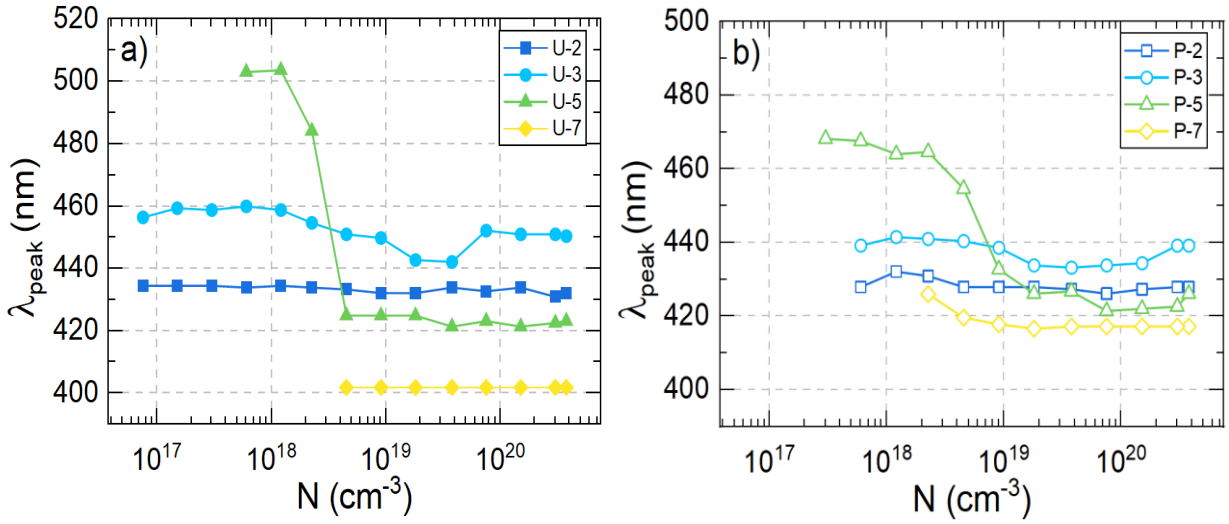

Figure 14. λ_{peak} dependence on photogenerated carrier density for a) u-GaN and b) p-GaN cap SQWs.

Compared to the u-GaN capped structures, the p-GaN capped samples exhibit smaller spectral shifts and less pronounced peak separation. This behavior likely indicates partial suppression of the internal polarization fields through the incorporation of the p-GaN cap layer. Ionized Mg acceptors introduced in the p-GaN may partially compensate or screen the built-in piezoelectric fields, thereby reducing band bending and weakening the QCSE.

The emission peak also exhibits an "S-shaped" dependence on carrier density. At low carrier densities, carriers relax randomly into both shallow and deep localized states. As the carrier density increases from $10^{17}$to 10^{18} cm^{-3}, a red shift in the emission peak is observed, which is attributed to carriers transitioning from shallow localized states into deeper localized states. At intermediate carrier densities (10^{18} to 10^{19} cm^{-3}), a blue shift occurs due to band-tail filling and screening of the quantum-confined Stark effect (QCSE) caused by the increased carrier population. Interestingly, when the carrier density approaches 10^{20} cm^{-3}, the emission peak shifts to lower energies again. This secondary red shift is attributed to bandgap renormalization, proposed by the previous studies [35].

These transitions between dominant recombination pathways are reflected in the FWHM trends aswell (Figure 15). U-3 exhibits a broad FWHM (up to 50 nm) due to the overlapping contributions of poorly separated peaks. In contrast, U-5 shows a definitive narrowing of the emission with peak shifting from 510 to 420 nm at $10^{19}cm^{-3}$ nm as a result of filling of localized states in In-rich area, with delocalized states becoming dominant. For U-7 and P-7 samples, afore mentioned strain relaxation events reduce the FWHM down to 20 nm for both samples, allowing less spectral disorder.

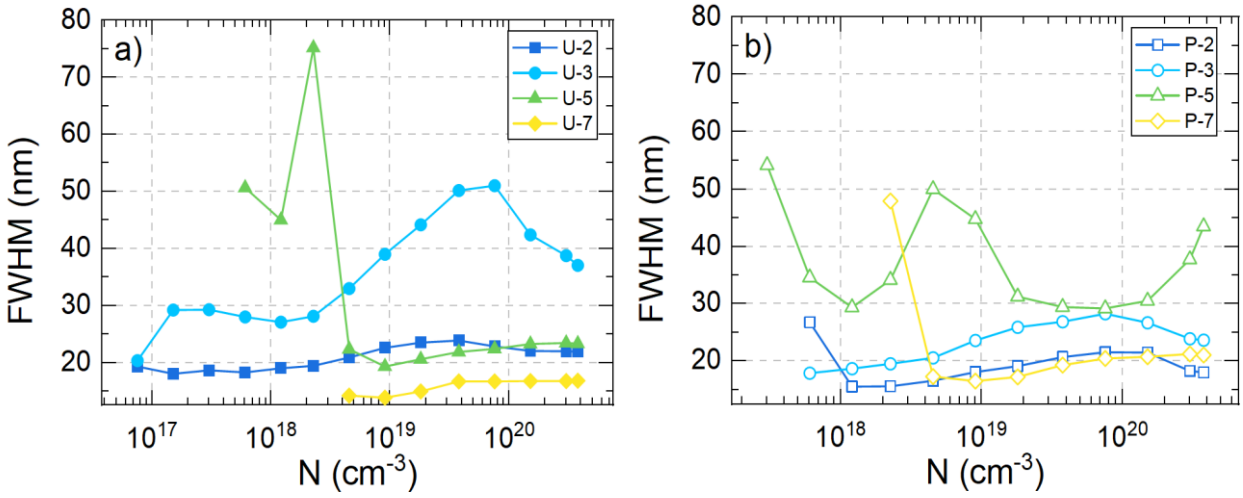

Figure 15. FWHM dependence on photogenerated carrier density for a) u-GaN and b) p-GaN cap SQWs.

5.1.1 QE Findings

To estimate the overall efficiency of the SQWs, QE measurements were performed using integrating sphere with 3 measurement approach under an excitation fluence of 500 μJ/cm². Calculated QE values using equation (13) against QW width are presented in Figure 16. A divergence in efficiency trends was observed between the two capping regimes. For the u-GaN capped samples, QE was found to be highest in narrow wells U-2 (7.6%) and U-3 (7%) but degraded significantly down to 3.9% (U-7 sample) as the QW width increased, a result of the reduced electron-hole wavefunction overlap caused by the increased QCSE in thicker wells. Conversely, while the p-GaN capped samples exhibited lower initial efficiency in the P-2 (3%) sample, they maintained a stable QE of ~ 4.3% across the broader QW width range, values slightly better than what was observed in their u-GaN counterparts. This suggests that the p-GaN layer may be facilitating internal field compensation, mitigating the negative effects of polarization and preserving radiative recombination rates even as the physical dimensions of the active region increase.

From QE measurements, using equation (14) direct absorption (A_{dir}) values were also extracted. It was observed that A_{dir} linearly increased from 38% to 46%, as QW width increased. As the only parameter that changes is the width of SQW, the increase may be attributed to the contribution of active layers with increasing thickness of QW width.

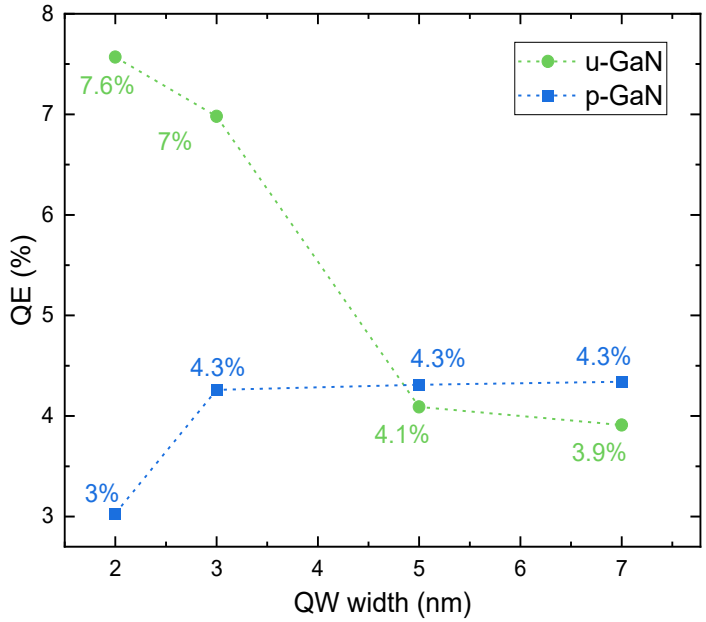

Figure 16. QE of u-GaN and p-GaN cap SQWs at 500 uJ/cm^2.

Since the efficiency in InGaN-based structures exhibits a nonlinear dependence on carrier density, comparison at a single fluence is insufficient. Therefore, the time-integrated photoluminescence (TIPL) spectra were integrated and normalized by the excitation fluence to obtain a relative efficiency metric. This metric was subsequently scaled using the reference QE value obtained at 500 μJ/cm² to enable comparison across samples and to assess the dominant recombination pathways. The resulting efficiency as a function of carrier density is presented in Figure 17.

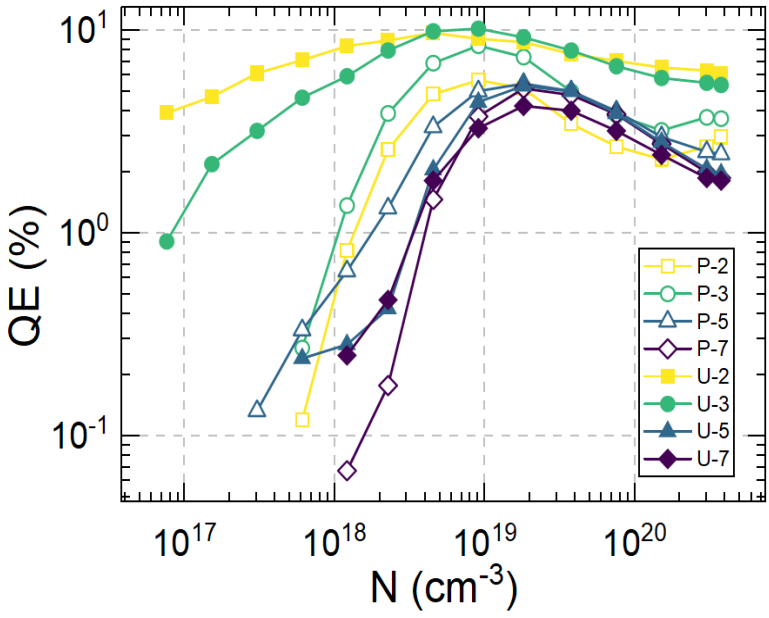

Figure 17. QE dependence on photogenerated carrier density for all samples.

It can be observed that the U-2 and U-3 samples exhibit the highest efficiencies among all investigated structures, with peak QE reaching 9.1% and 10.2%, respectively. In addition to their higher peak efficiencies, these samples display a distinct carrier-density-dependent recombination behavior. At carrier densities below approximately 9.1×10^{18} cm^{-3}, the QE slope is noticeably less steep compared to the other samples, indicating that bimolecular radiative recombination is the dominant recombination mechanism in this regime.

In contrast, the remaining samples exhibit a significantly steeper slope at low carrier densities, which is characteristic of SRH non-radiative recombination. Furthermore, the influence of SRH recombination becomes increasingly pronounced with increasing QW width. This trend is physically reasonable, as wider QWs are generally associated with increased defect formation and a higher density of TDs. The reduced electron–hole wavefunction overlap in wider QWs, caused by QCSE, may also contribute to the reduced radiative recombination efficiency.

The QE maximum for most samples occurs near 9.1×10^{18} cm^{-3}, while for the 5 nm and 7 nm QW samples the peak shifts slightly toward higher carrier densities, approaching 10^{19} cm^{-3}. Beyond the QE peak, efficiency droop is observed, which is commonly attributed to Auger–Meitner recombination. However, the U-2 and U-3 samples demonstrate comparatively weaker droop behavior, indicating reduced susceptibility to Auger-related non-radiative losses. The improved performance of these samples is likely related to enhanced carrier confinement and stronger electron–hole overlap, which together increase the probability of radiative bimolecular recombination while suppressing competing non-radiative pathways. Interestingly, this behavior is not observed in the corresponding p-cap structures, although their efficiencies remain superior to those of the larger QW width samples. This degradation in performance may be attributed to the diffusion of ionized Mg atoms into the active region, introducing additional non-radiative recombination centers or Mg-related defect complexes, potentially involving N_V, which negatively affect carrier localization and recombination dynamics [36]. However, at larger QW widths, the p-cap samples still exhibit comparable or slightly improved performance, particularly at high carrier densities, possibly because Mg-related defects do not penetrate as deeply into the wider quantum well active regions. Considering previous studies have shown that Mg diffusion at typical p-GaN growth temperatures can be on the order several nanometers for standard growth conditions and extended at elevated growth and RTA conditions, Mg leakage into active regions is considered plausible for the current samples [37].

Evaluation of Real IQE

It is likely that the A_{dir} coefficients obtained using the three-measurement approach are overestimated. According to previous studies, the A_{dir} coefficient for InGaN QW structures is typically expected to be of smaller order [38]. In the present case, however, the extracted A_{dir} values exceed 40%, indicating the presence of significant parasitic absorption from surrounding layers and scattering from the rough substrate. One probable explanation is the partial excitation of adjacent u-GaN layers, since the excitation wavelength is relatively close to the GaN band edge.

A systematic increase in $A_{dir}$with increasing SQW width is also observed. Since the only structural parameter varied between these samples is the QW thickness, the measured change in empirical A_{dir} values can reasonably be attributed to the contribution of the active region itself. Therefore, the effective absorption coefficient may be expressed as:

$$A_{effective} = A_{bg} + A_{QW}, \tag{21}$$

where A_{bg} represents the parasitic contribution originating from the surrounding epitaxial layers, while A_{QW} corresponds to absorption within the quantum well active region.

The contribution of $A_{QW}$was estimated empirically from the slope of the measured A_{dir} dependence on QW width. For this analysis, the A_{dir} values of u-GaN- and p-GaN-capped samples were averaged. The 7 nm SQW samples were excluded due to their different growth temperature conditions, which may promote In segregation and introduce additional uncertainties. The extracted results indicate that the active-region contribution increases by approximately 1.8% per nanometer of QW thickness, as shown in Figure 18.

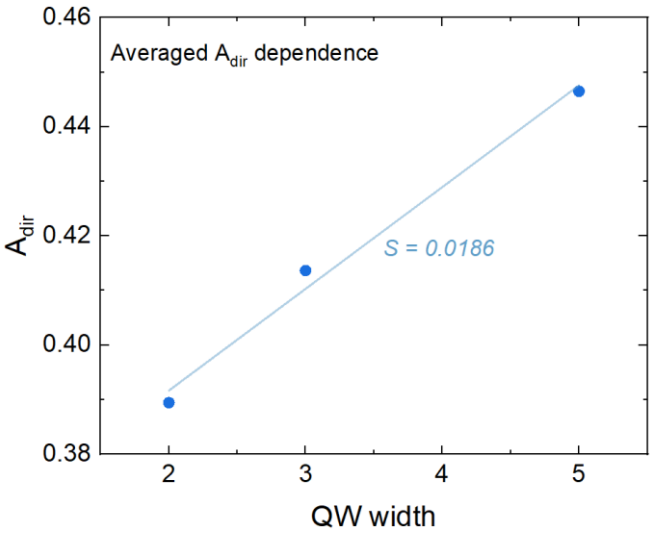

Figure 18. Dependence of direct absorption on QW width.

The contribution of active layer to absorption can further be validated with the prediction of the Beer–Lambert law:

$$A = 1 - e^{-\alpha d} \tag{22}$$

Assuming $\alpha = 1.5 \times 10^5$ cm^{-1}at 385 nm, the expected absorption increase for an additional 1 nm of active-region thickness is approximately 1.5%, which closely matches the experimentally extracted value. The larger absorption increase observed for thinner wells (2.1% between 2–3 nm) compared to thicker wells (1.5% between 3–5 nm) also suggests enhanced oscillator strength due to stronger quantum confinement. As QW width increases, reduced electron–hole wavefunction overlap caused by QCSE lowers the absorption cross-section per unit volume. Nevertheless, the influence of wavefunction overlap remains relatively minor compared to the direct contribution of increasing active-region thickness.

The corrected IQE results obtained after accounting for the active-layer contribution are shown in Figure 19. For the p-GaN-capped samples, the peak IQE values of P-2, P-3, P-5, and P-7 increase from 5.6%, 8.45%, 5.5%, and 5.2% to 69.2%, 44.8%, 27.7%, and 20.3%, respectively. Such values are consistent with reported efficiencies for InGaN QWs with moderate indium compositions [39] [40]. The u-GaN-capped samples exhibit even higher corrected IQEs, with U-2, U-3, U-5, and U-7 reaching approximately 95%, 60.7%, 27%, and 17.1%, respectively.

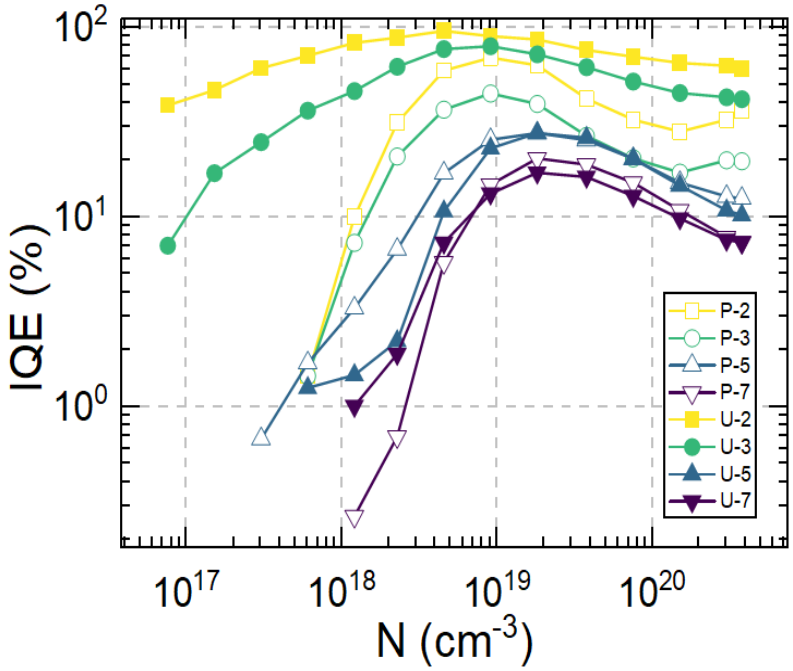

Figure 19. IQE dependence on photogenerated carrier density.

5.2 LITG Results

LITG measurements were conducted over a fluence range of 30–320 µJ/cm² using nine distinct grating periods spanning 1.99–3.89 µm (after conversion for the reflection-mode configuration described in Chapter 4.3). Measurements were performed exclusively in reflection mode, as transmission-mode measurements were not compatible with the patterned substrate samples.

Prior to measurement, all samples underwent extended polishing using a UNIPOL300 polishing machine for up to 16 hours in order to minimize substrate-induced scattering and improve signal quality. This preparation enabled reliable signal acquisition from the 5 and 7 QW structures. In contrast, the signal intensity obtained from the 2 and 3 nm QW samples remained comparable to the background level under the employed measurement conditions and could not be extracted. As an illustrative example, the LITG decay as a function of delay time for samples U-5 and P-5 at a grating period of 1.99 µm is shown in Figure 20. The decay dynamics of both samples exhibit a similar temporal behavior, indicating comparable carrier relaxation kinetics under these measurement conditions accompanied by increasing decay rate with the excitation fluence, which is an indication of higher order recombination mechanisms taking place.

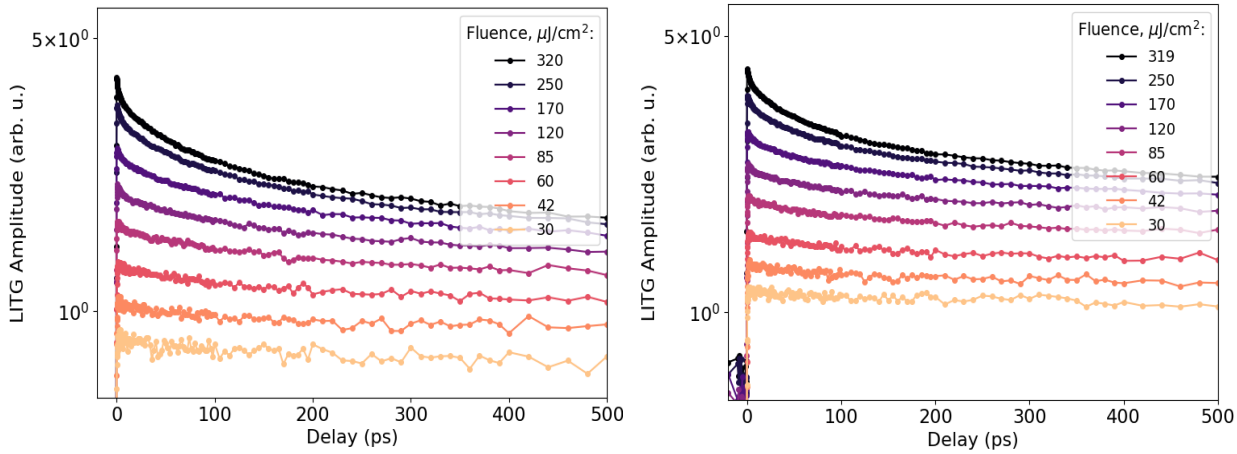

Figure 20. LITG decay kinetics U-5 (left) and P-5 (right) sample at 1.99 µm grating period.

Figure 21 shows the diffusivity as a function of carrier density for the investigated samples. All samples exhibit comparable diffusivity values ranging from approximately 0.2 to 2.5 cm²/s and a similar increase in diffusivity with increasing carrier density. No strong dependence of diffusivity on QW width or cap layer type was observed. Although the U-5 and P-5 samples exhibit slightly higher diffusivity values (2.6 cm²/s and 2.3 cm²/s, respectively) at elevated carrier densities compared to the P7 and U7 (~1.9 cm²/s) samples, the overall differences remain relatively small. The comparable diffusivity observed for all structures indicates that lateral carrier transport is

dominated mainly by carrier localization and ambipolar transport effects. The effective carrier mobility can be estimated from the experimentally measured ambipolar diffusivity using the Einstein relation:

$$D = \frac{kT\mu}{e} \tag{23}$$

where D is the diffusivity, k is the Boltzmann constant, T is the absolute temperature, e is the elementary charge, and μ is the carrier mobility. At room temperature, the relation simplifies to:

$$\mu \approx \frac{D}{0.0259} \tag{24}$$

Using the experimentally observed diffusivity values, the corresponding effective carrier mobility was estimated to range from approximately 7.7 to 96.5 cm²/V·s. Since the LITG technique measures the ambipolar diffusion coefficient, the extracted mobility values represent effective ambipolar mobilities rather than purely electron mobilities. Under low-injection conditions in n-type materials, ambipolar transport is expected to be limited primarily by the lower-mobility minority carriers (holes). Therefore, the lower-density mobility values may provide an approximate indication of hole transport properties in the investigated samples. The obtained diffusivity and mobility values are comparable to previously reported results in GaN-based materials measured using optical diffusion techniques [41] [42].

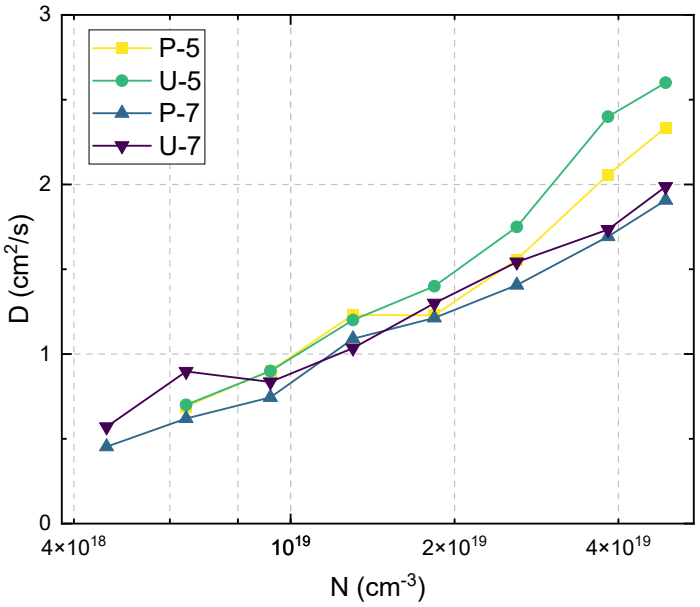

Figure 21. Diffusivity of the samples as a function of photogenerated carrier density.

Carrier lifetimes were also extracted for the investigated samples. Determination of lifetime values using the LITG technique was challenging due to the relatively long recombination lifetimes of the InGaN QWs, combined with the reflection-mode measurement configuration and the resulting low signal intensity. Therefore, lifetime extraction was performed under pump–probe-like conditions using the largest accessible grating periods in order to minimize the influence of carrier diffusion on the transient decay. The extracted lifetime values as a function of carrier density are presented in Figure 22.

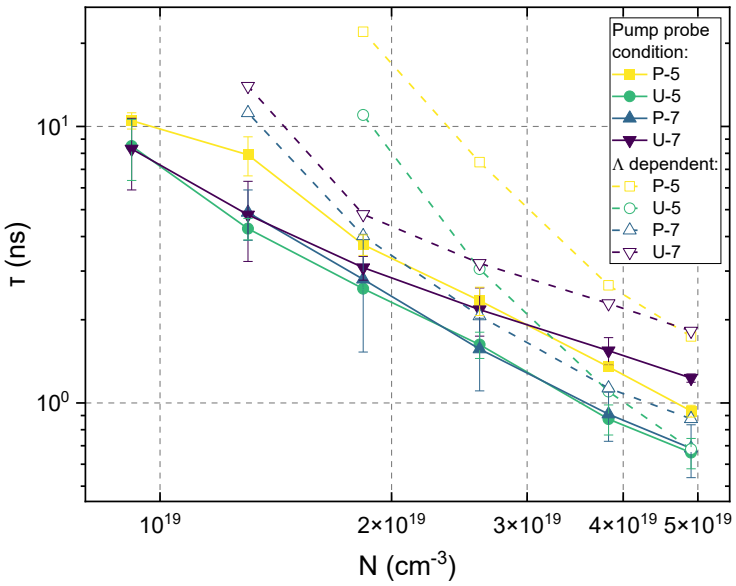

Figure 22. Pump probe condition and angular dependence LITG lifetimes of the samples as a function of photogenerated carrier density.

All samples exhibit similar lifetime behavior over the investigated carrier density range. At low carrier densities ($\sim 9 \times 10^{18}$ cm^{-3}), relatively long lifetimes in the range of approximately 8–10 ns are observed, which can be attributed to strong carrier localization in the InGaN quantum wells. As the photogenerated carrier density increases, the carrier lifetime decreases progressively to approximately 0.6–0.8 ns. This reduction is likely associated with carrier delocalization and enhanced recombination resulting from screening of localized potential fluctuations and internal electric fields at elevated excitation densities.

No clear dependence of carrier lifetime on cap doping or QW width was observed. The similar lifetime behavior across all investigated structures suggests that carrier recombination and transport are governed primarily by common localization and disorder-related mechanisms, while any modifications arising from changes in polarization fields or quantum confinement remain comparatively weak within the investigated parameter range. Lifetime was also extracted using all

grating periods to see if there were any changes. A slight tendency toward longer lifetimes was observed for the 5 nm QW samples at lower carrier densities in the Λ-dependent LITG measurements. This behavior may indicate somewhat enhanced carrier localization in the narrower wells. However, since lifetime extraction under these measurement conditions was experimentally challenging and associated with increased uncertainty, this trend should be interpreted cautiously.

Finally, diffusion length (L_D) was calculated using equation (19) from diffusivity and pump-probe condition LITG lifetimes and plotted against carrier density in Figure 23. All samples exhibit a similar decrease in diffusion length with increasing carrier density, with L_D decreasing from approximately 0.85–0.88 μm at low carrier densities to approximately 0.35–0.50 μm at the highest excitation densities. The reduction in diffusion length is mainly driven by the strong decrease in carrier lifetime at elevated carrier densities, which outweighs the simultaneous increase in diffusivity. Consequently, although carrier transport becomes more efficient at high excitation densities, the shorter recombination times limit the overall diffusion distance.

Only minor differences between the investigated structures were observed. The U-7 sample exhibits slightly larger diffusion lengths at higher carrier densities, primarily due to its comparatively longer carrier lifetime in this regime. Overall, the comparable diffusion length behavior among all samples indicates that variations in QW width and cap layer type have only a limited influence on the effective lateral carrier transport within the investigated carrier density range.

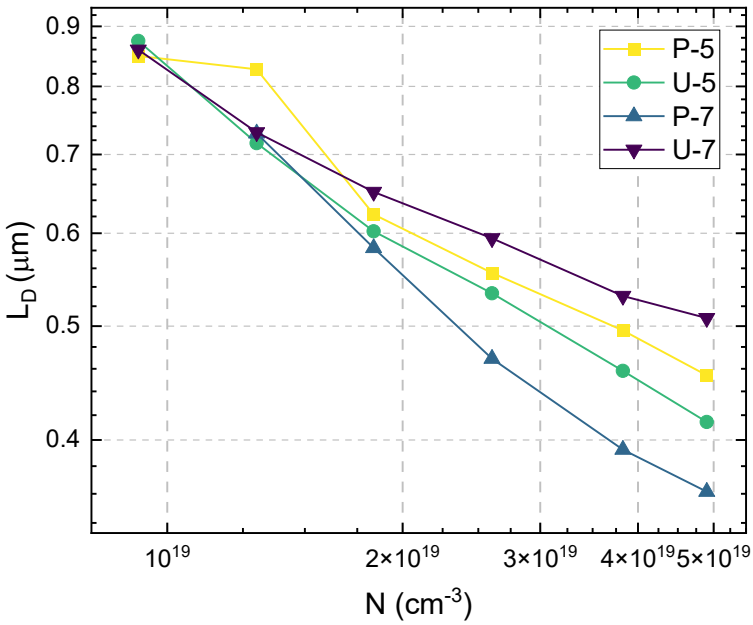

Figure 23. Diffusion length of the samples as a function of carrier density.

5.3 ABC Modelling

5.3.1 ABC Modelling on Raw Data

The extended AB*C model described in Section 2.1.1 was applied to the investigated samples by varying the parameters τ_{n_0}, τ_{p_0}, $B_{0\mathrm{rad}}$, B_{TAAM}, n_{sat}, n_{SRH}, n_0, and C. Equal electron and hole SRH lifetimes were assumed ($\tau_{n_0} = \tau_{p_0}$), giving an effective SRH lifetime of $\tau_{SRH} = 2\tau_{n_0}$. Similarly, equal Auger-Meitner coefficients for electrons and holes were assumed ($C_n = C_p$), resulting in $C = 2C_n$. The parameters n_{sat} and n_{SRH} account for the saturation behavior of the bimolecular and SRH recombination channels, respectively. The model was fitted simultaneously to the experimental LITG lifetime and TIPL QE data. The resulting fits for the U-5 and P-5 samples are presented in Figure 24 and the extracted model parameters for all samples are summarized in Table 2.

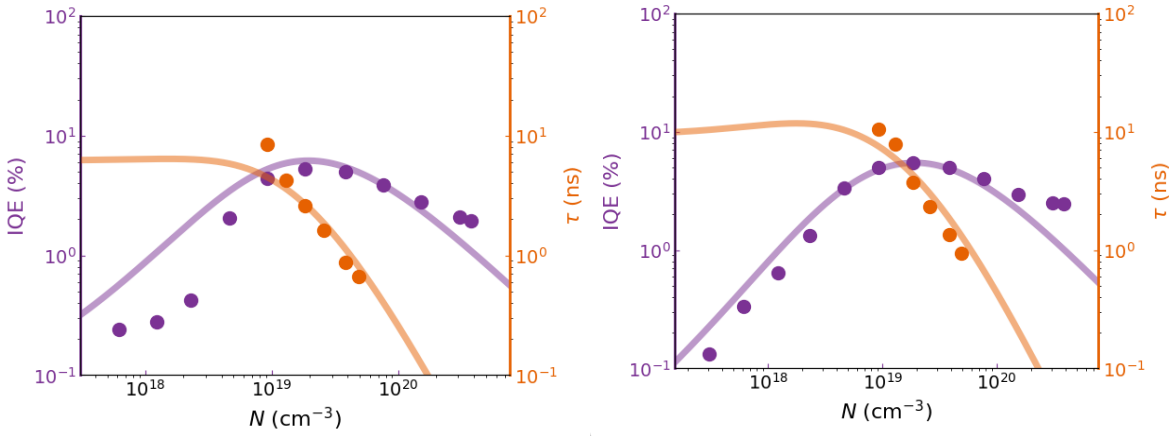

Figure 24. AB*C modelling with QE data for U-5 (left) and P-5 (right) samples

Table 2. AB*C parameters of fitted LITG lifetime and QE values

Sample	τ_{SRH} (ns)	B_{rad} (cm^3/s)	B_{TAAM} (cm^3/s)	n_{SRH} (cm^{-3})	n_{sat} (cm^{-3})	n_0 (cm^{-3})	C (cm^6/s)
U-5	13	1×10^{-12}	8×10^{-12}	8×10^{18}	-	1×10^{17}	1.3×10^{-31}
P-5	18	1×10^{-12}	9×10^{-12}	8×10^{18}	-	1×10^{16}	9×10^{-32}
U-7	13.5	8×10^{-13}	6.5×10^{-12}	8×10^{18}	-	1×10^{17}	9.5×10^{-32}
P-7	9	1×10^{-12}	9.2×10^{-12}	8×10^{18}	-	1×10^{16}	1.1×10^{-31}

The simultaneous fitting of QE and carrier lifetimes severely restricts the model parameters, revealing a critical discrepancy in the low carrier density regime. The low-efficiency tail for both U-5 and P-5 samples is governed by the effective SRH lifetime and its saturation behavior. There

was no saturation for B_{rad} for the samples, so n_{sat} was not used in the fitting. Unlike simple ABC models that treat the SRH lifetime as a fixed coefficient, the present extended model introduces SRH saturation density (n_{SRH}) as an important parameter, which was kept nearly constant at ~8×10^{18} for most samples, a value that correlates with what is observed in QE against carrier density plots. Despite accounting for this saturation, the fitting plots show that the QE at low carrier densities is severely overestimated, an effect that is particularly pronounced for both u-GaN cap samples. A fitting compromise was required to account for lifetimes correctly as well, since forcing a steeper QE slope in the low carrier density range would result in severely reduced lifetimes that do not match the lack of a lifetime reduction onset in the experimental data. Given that low-density lifetimes were difficult to extract precisely, prioritizing a more accurate QE fit at this stage is considered essential for extracting reliable recombination coefficients.

Comparing the 5 nm QW structures, the introduction of p-GaN cap (P-5) over u-GaN cap (U-5) increases the non-radiative SRH lifetime τ_{SRH} from 13 ns to 18 ns while dropping the background electron density (n_0) by an order of magnitude from 1×10^{17} to 1×10^{16} cm^{-3}. This behavior supports the hypothesis that p-type doping introduces acceptor states that electrostatically compensate native donor defects, possibly through the formation of neutral Mg–V_N complexes. Furthermore, the P-5 sample displays slightly suppressed Auger-Meitner recombination coefficient ($C = 9\times10^{-32}$ cm^6/s compared to 1.3×10^{-31} cm^6/s for U-5), making it more resilient to efficiency droop at higher carrier concentrations.

In the u-GaN cap series, widening the well causes B_{rad} to drop from 1×10^{-12} cm^3/s for U-5 to 8×10^{-13} cm^3/s for U-7, which is a direct consequence of reduction of wavefunction overlap. However, in the p-capped series, the radiative coefficient remains stable at 1×10^{-12} cm^3/s for both the P-5 and P-7 structures, suggesting that the p-type layer provides a degree of electrostatic screening that counteracts the internal piezoelectric fields in the thicker well. At the same time, a drop of SRH lifetime down to 9 ns is observed.

A notable characteristic of the entire parameter set in Table 2 is that B_{rad} and B_{TAAM} coefficients are consistently lower than values typically reported in the literature for InGaN QW structures. This is a direct consequence of absorption, scattering and extraction losses that come with QE, which forces the fitting routine to artificially suppress both the radiative and non-radiative coefficients to maintain a mathematical balance with the lifetime data. To extract physically accurate absolute recombination coefficients, the real, absolute IQE values must be rigorously accounted for in the model calibration.

5.3.2 ABC Modelling of corrected IQE Values

AB*C modelling was also applied to samples upon IQE correction for more accurate modelling. Fitting for U-5 and P-5 samples using the IQE values from active layer contribution are represented in Figure 25 with resulting parameters in Table 3.

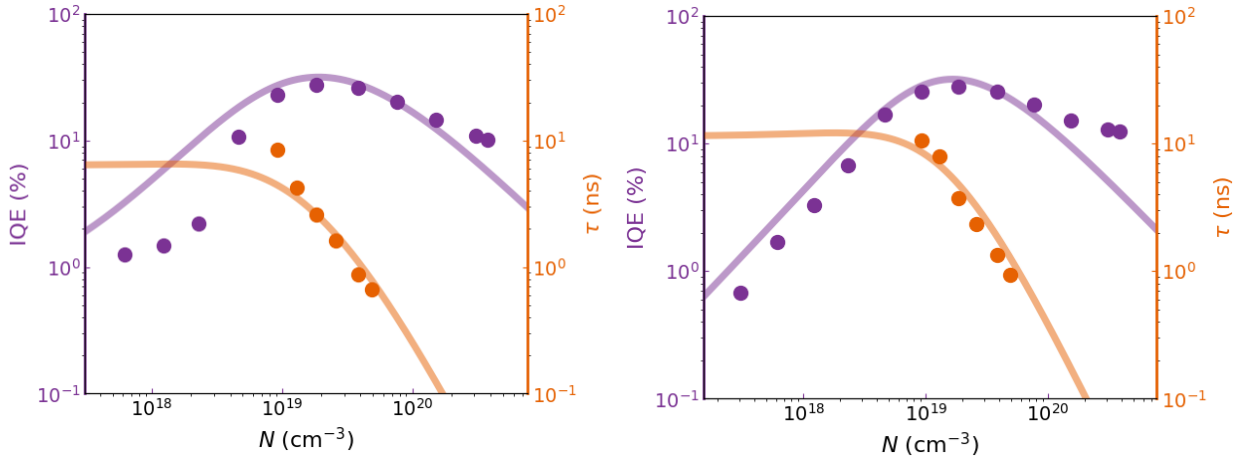

Figure 25. AB*C modelling with IQE data for U-5 (left) and P-5 (right) samples

Table 3. AB*C parameters of fitted LITG lifetime and IQE values.

Sample	τ_{SRH} (ns)	B_{rad} (cm^3/s)	B_{TAAM} (cm^3/s)	n_{SRH} (cm^{-3})	n_{sat} (cm^{-3})	n_0 (cm^{-3})	C (cm^6/s)
U-5	13	6.5×10^{-12}	4.3×10^{-12}	8×10^{18}	-	1×10^{17}	1.3×10^{-31}
P-5	19	4.9×10^{-12}	2×10^{-12}	8×10^{18}	-	1×10^{16}	1×10^{-31}
U-7	13.5	3.4×10^{-12}	3×10^{-12}	8×10^{18}	-	1×10^{17}	1.1×10^{-31}
P-7	8.4	4.5×10^{-12}	6×10^{-12}	8×10^{18}	-	1×10^{16}	1.1×10^{-31}

Shifting the IQE curves upward only affect the extracted $B_{\mathrm{rad}}$and B_{TAAM}contributions, while other parameters remain similar. Therefore, afore mentioned analysis for previous parameters hold, and effects of QW width and doping change are compared in terms of these coefficients. As illustrated in the extracted parameter histograms (Figure 26), the corrected IQE analysis increases the obtained B_{rad}values into the mid-10^{-12} cm^3/s range, bringing them significantly closer to values commonly reported in the literature for InGaN QWs and reducing the artificial parameter compression introduced in QE fits by the extraction-related reduction [43]. Consequently B_{TAAM}

values decrease upon the IQE correction, as both contributions scale with the same order with respect to carrier density.

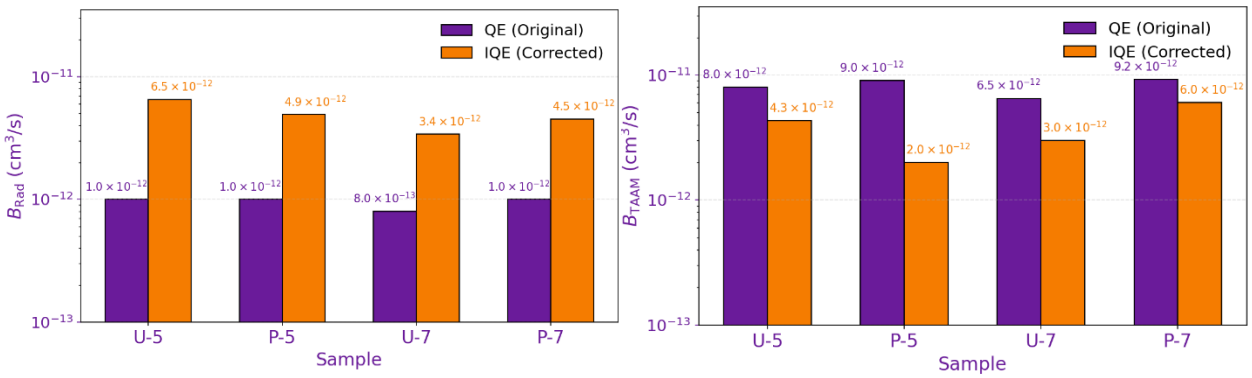

Figure 26. Extracted B_{rad}(left) and B_{TAAM} (right) values with QE and IQE correct ABC modelling

Comparing the samples in terms of QW width with new parameters, when the QW width is increased from 5 to 7 nm in the U-7 sample, the wider well causes a substantial reduction in the radiative coefficient, decreasing from 6.5×10^{-12} to $3.4 \times 10^{-12}\mathrm{cm}^3/\mathrm{s}$ as a result of increased QCSE and electron–hole wavefunction separation. In contrast, in p-GaN capped samples, reduction is much less pronounced, going from $4.9 \times 10^{-12}\mathrm{cm}^3/\mathrm{s}$ in P-5 sample to $4.3 \times 10^{-12}\mathrm{cm}^3/\mathrm{s}$ in P-7. This suggests that internal piezoelectric field in p-GaN capped structures may be effectively screened, restoring the radiative coefficient. However, this is accompanied by a severe deterioration in material quality, evidenced by a sharp reduction in the SRH lifetime to 8.4 ns, indicating enhanced defect formation at the interface between the wider quantum well and the doped cap layer by Mg atoms.

In contrast to the consistent trends observed in B_{rad}, variations in B_{TAAM} are less systematic and therefore more difficult to interpret quantitatively. For 5 nm QW structures, B_{TAAM} decreases from $4.3 \times 10^{-12}$to $2.0 \times 10^{-12}\ \mathrm{cm}^3/\mathrm{s}$, accompanied by a reduction in the C coefficient, which is consistent with the stronger efficiency droop observed in U-5 relative to P-5 in the IQE analysis. However, for 7 nm QWs, B_{TAAM}increases from $3.0 \times 10^{-12}$to $6.0 \times 10^{-12}\ \mathrm{cm}^3/\mathrm{s}$ following introduction of the p-GaN cap layer. Since this behavior does not follow the same systematic trend as B_{rad}, these values should be interpreted cautiously and may reflect fitting sensitivity rather than a physically robust trend.

6 Conclusions

- A progressive increase in SQW width led to the formation of double emission peaks in the PL spectra. The second peak that appears at longer wavelengths is attributed to formation of In rich clusters during growth, and the onset of double emission peak was 3 nm SQW width.

- Samples with a p-GaN cap layer exhibited comparatively higher QE values at larger SQW widths than their u-GaN counterparts, illustrating the positive effect of the p–n junction field in screening internal polarization fields and sustaining efficiency in wider SQW structures.

- Introduction of p-GaN cap layer severally reduces QE for lower SQW widths compared to their u-GaN cap equivalents. This reduction is likely associated with Mg diffusion into the active region.

- Although both SQW width and cap-layer configuration affected the PL spectra and spectral shifts, the measured transport parameters remained nearly unchanged among the samples. This indicates that variations in internal electric fields have minimal influence on carrier transport properties.

7 Summary

This thesis was prepared by Seda Türkcan (academic supervisor—dr. Kazimieras Nomeika) under the title “Carrier Dynamics in n-GaN/InGaN/p-GaN Structures with Different Active Layer Widths” at Vilnius University, Institute of Photonics and Nanotechnology. The work investigates non-equilibrium charge carrier dynamics and internal quantum efficiency (IQE) in InGaN single quantum well (SQW) structures with varying active layer widths and cap-layer doping configurations. The main objective was to investigate how SQW width and cap doping influence recombination mechanisms, efficiency, and carrier transport properties in InGaN/GaN heterostructures.

The study was carried out using Light-Induced Transient Grating (LITG) and Time-Integrated Photoluminescence (TIPL) techniques. Eight SQW samples—U-2, U-3, U-5, U-7, P-2, P-3, P-5, and P-7—were analyzed, where the labels represent the QW width and cap-layer type. The experimental results showed that increasing the SQW width led to the appearance of double emission peaks in the photoluminescence spectra, with the secondary long-wavelength peak attributed to the formation of In-rich clusters. This effect became evident for SQW widths of 3 nm and above.

The optical analysis further demonstrated that samples incorporating a p-GaN cap layer exhibited comparatively higher QE values at larger SQW widths than their u-GaN counterparts. This behavior indicates that the p–n junction field partially screens internal polarization fields, thereby reducing the impact of the quantum-confined Stark effect (QCSE) and helping sustain radiative efficiency in wider SQW structures. However, the introduction of the p-GaN cap layer significantly reduced QE in narrower SQW structures, likely due to Mg diffusion into the active region and the resulting increase in defect-related non-radiative recombination.

Although both SQW width and cap-layer configuration strongly influenced the photoluminescence spectra and spectral shifts, the measured carrier transport parameters remained nearly unchanged among the investigated samples. This suggests that variations in internal electric fields have only a limited influence on carrier transport properties within the studied structures. Overall, the results provide insight into the competing effects of QCSE screening and defect formation in InGaN/GaN SQW systems and contribute to the optimization of quantum well designs for high-efficiency optoelectronic devices.

8 References

[1] Narukawa, Y. (2010). White light emitting diodes with super-high luminous efficacy. Appl. Phys., 43 (354002).

[2] Bernardini, F. (1999). Spontaneous versus piezoelectric polarization in III–V nitrides: conceptual aspects and practical consequences. physica status solidi (b), 216(1), 391-398.

[3] Hajdel, M (2021). Dependence of InGaN quantum well thickness on the nature of optical transitions in LEDs. Materials, 15(1), 237.

[4] Nomeika, K. (2022). Impact of carrier diffusion on the internal quantum efficiency of InGaN quantum well structures. Journal of Materials Chemistry C, 10(5), 1735-1745.

[5] Nomeika, K. (2019). Novel ways of improving quantum efficiency of InGaN LED active layers by controlling carrier diffusivity. (Doctoral dissertation, Vilniaus universitetas.).

[6] Hader, J. (2005). Supression of carrier recombination in semiconductor lasers by phase-space filling. Applied Physics Letters, 87(20).

[7] Kour, R. (2019). Recent advances and challenges in indium gallium nitride (inxga1-xn) materials for solid state lighting. ECS Journal of Solid State Science and Technology, 9(1), 015011., 1-2.

[8] Barrett, R. (2023). Investigating carrier dynamics in InGaN/GaN quantum wells. The University of Manchester (United Kingdom).

[9] Wu, M. (2000). Elastic strain in InGaN and AlGaN layers. Materials Science and Engineering: B, 75(2-3), 232-235.

[10] Miskys, C. (2004). New Substrates for Epitaxy of Group III Nitride Semiconductors: Challenges and Potential. (Doctoral dissertation, Technische Universität München).

[11] Melton, W. (1997). GaN growth on sapphire. Journal of crystal growth, 178(1-2), 168-173.

[12] Hangleiter, A. (2005). Suppression of nonradiative recombination by V-shaped pits in GaInN/GaN quantum wells produces a large increase in the light emission efficiency. Physical review letters, 95(12), 127402.

[13] Wang, X. (2012). Wang, X., Liu, S., Ma, N., Feng, L., Chen, G., Xu, F., ... & Shen, B. (2012). High-electron-mobility InN layers grown by boundary-temperature-controlled epitaxy. Applied Physics Express, 5(1), 015502., 1.

[14] Chichibu, S. (1996). pontaneous emission of localized excitons in InGaN single and multiquantum well structures. Applied Physics Letters, 69(27), 4188-4190.

[15] Inatomi, Y. (2017). Theoretical study of the composition pulling effect in InGaN metalorganic vapor-phase epitaxy growth. Japanese Journal of Applied Physics, 56(7), 078003.

[16] Stringfellow, G. (2010). Microstructures produced during the epitaxial growth of InGaN alloys. Journal of Crystal Growth, 312(6), 735-749.

[17] Sheu, J. (2002). Thedoping process and dopant characteristics of GaN. Journal of Physics: Condensed Matter, 14(22), R657.

[18] Reshchikov, M. (2005). Luminescence properties of defects in GaN. Journal of applied physics, 97(6).

[19] Nakamura, S. (1992). Si- and Ge-Doped GaN Films Grown with GaN Buffer Layers. Japanese Journal of Applied Physics, vol. 31, pp. 2883-2888.

[20] Amano, H. (1989). P-type conduction in Mg-doped GaN treated with low-energy electron beam irradiation (LEEBI). Japanese journal of applied physics, 28(12), L2112-L2114.

[21] Fiorentini, V. (1999). Effects of macroscopic polarization in III-V nitride multiple quantum wells. Physical Review B, 60(1).

[22] Park, S. (1999). Crystal-orientation effects on the piezoelectric field and electronic properties of strained wurtzite semiconductors. Physical Review B, 59(7), 4725.

[23] Takeuchi, T. (2000). Theoretical study of orientation dependence of piezoelectric effects in wurtzite strained GaInN/GaN heterostructures and quantum wells. Japanese Journal of Applied Physics, 39(2R), 413.

[24] Fichtenbaum, N. (2007). Electrical characterization of p-type N-polar and Ga-polar GaN grown by metalorganic chemical vapor deposition. Applied Physics Letters, 91(17).

[25] Park, S. (2011). Optical properties of staggered InGaN/InGaN/GaN quantum-well structures with Ga-and N-faces. Japanese journal of applied physics, 50(7R), 072101.

[26] Ji, Y. (2022). Alleviated built-in electric field in the active region of AlGaN deep-ultraviolet light-emitting diodes with locally embedded pin junctions. Applied Optics, 61(24), 6961-6966.

[27] Saranya, G. (2025). Effect of p-GaN layer and High-k material in InGaN/GaN LED for optical performance enhancement. Journal of Optics, 54(4), 1595-1603.

[28] Zhou, X. (2017). Surface morphology evolution mechanisms of InGaN/GaN multiple quantum wells with mixture N2/H2-grown GaN barrier. Nanoscale Research Letters, 12(1), 354.

[29] Leyre, S. (2014). Absolute determination of photoluminescence quantum efficiency using an integrating sphere setup. Review of scientific instruments, 85(12).

[30] Eichler, H. (2013). Laser-induced dynamic gratings (Vol. 50). Springer.

[31] Chen, Z. Z. (2007). The origins of double emission peaks in electroluminescence spectrum from InGaN/GaN MQW LED. Journal of crystal growth, 298, 731-735.

[32] Pozina, G. B. (2000). Origin of multiple peak photoluminescence in InGaN/GaN multiple quantum wells. Journal of Applied Physics, 88(5), 2677-2681.

[33] Zhu, J. (2009). The investigation on strain relaxation and double peaks in photoluminescence of InGaN/GaN MQW layers. Journal of Physics D: Applied Physics, 42(23), 235104.

[34] Kazazis, S. (2017). Polarization-Engineered InGaN/GaN Heterojunctions for Photovoltaic Applications. arXiv preprint arXiv:1709.03729.

[35] Nomeika, K. (2017). Impact of carrier localization and diffusion on photoluminescence in highly excited cyan and green InGaN LED structures. Journal of Luminescence, 188, 301-306.

[36] Zhang, N. (2016). Effect of back diffusion of Mg dopants on optoelectronic properties of InGaN-based green light-emitting diodes. Chinese Physics Letters, 33(11), 117302.

[37] Romanov, I. (2018). Diffusion of magnesium in led structures with InGaN/GaN quantum wells at true growth temperatures 860–980° C of p-GaN. Russian Physics Journal, 61(1), 187-190.

[38] Ambacher, O. (1998). Absorption of InGaN single quantum wells determined by photothermal deflection spectroscopy. Japanese journal of applied physics, 37(3R), 745.

[39] Marcinkevičius, S. (2021). High internal quantum efficiency of long wavelength InGaN quantum wells. Applied Physics Letters, 119(7).

[40] Li, X. (2011). On the quantum efficiency of InGaN light emitting diodes: Effects of active layer design, electron cooler, and electron blocking layer. physica status solidi (a), 208(12), 2907-2912.

[41] Aleksiejūnas, R. (2003). Determination of free carrier bipolar diffusion coefficient and surface recombination velocity of undoped GaN epilayers. Applied physics letters, 83(6), 1157-1159.

[42] Olaizola, S. (2006). Time-resolved photoluminescence studies of carrier diffusion in GaN. Applied physics letters, 89(7).

[43] Wang, L. (2017). A review on experimental measurements for understanding efficiency droop in InGaN-based light-emitting diodes. Materials, 10(11), 1233.